Nano-Micro Letters

e-ISSN 2150-5551
CN 31-2103/TB

ARTICLE

https://doi.org/10.1007/s40820-025-01764-7

Cite as
Nano-Micro Lett.
(2025) 17:274

Received: 22 January 2025
Accepted: 8 April 2025

Machine Learning Tailored Anodes for Efficient Hydrogen Energy Generation in Proton-Conducting Solid Oxide Electrolysis Cells

Fangyuan Zheng[1], Baoyin Yuan[2], Youfeng Cai[1], Huanxin Xiang[1], Chunmei Tang[1,3] ✉, Ling Meng[1], Lei Du[1], Xiting Zhang[1], Feng Jiao[2], Yoshitaka Aoki[4], Ning Wang[1] ✉, Siyu Ye[1] ✉

HIGHLIGHTS

- Machine learning technique was employed to develop anode for proton-conducting solid oxide electrolysis cells (P-SOEC).
- The screened high-performance $La_{0.9}Ba_{0.1}Co_{0.7}Ni_{0.3}O_{3-\delta}$ (LBCN9173) and $La_{0.9}Ca_{0.1}Co_{0.7}Ni_{0.3}O_{3-\delta}$ (LCCN9173) anodes achieved a synergistic enhancement of water oxidation reaction kinetics and proton-conducting ability.
- P-SOECs with LBCN9173 anode demonstrated a top-rank current density of 2.45 A cm^{-2} and an extremely low polarization resistance of 0.05 Ω cm^2 at 650 °C.

ABSTRACT In the global trend of vigorously developing hydrogen energy, proton-conducting solid oxide electrolysis cells (P-SOECs) have attracted significant attention due to their advantages of high efficiency and not requiring precious metals. However, the application of P-SOECs faces challenges, particularly in developing high-performance anodes possessing both high catalytic activity and ionic conductivity. In this study, $La_{0.9}Ba_{0.1}Co_{0.7}Ni_{0.3}O_{3-\delta}$ (LBCN9173) and $La_{0.9}Ca_{0.1}Co_{0.7}Ni_{0.3}O_{3-\delta}$ (LCCN9173) oxides are tailored as promising anodes by machine learning model, achieving the synergistic enhancement of water oxidation reaction kinetics and proton conduction, which is confirmed by comprehensively analyzing experiment and density functional theory calculation results. Furthermore, the anodic reaction mechanisms for P-SOECs with these anodes are elucidated by analyzing distribution of relaxation time spectra and Gibbs energy of water oxidation reaction, manifesting that the dissociation of H_2O is facilitated on LBCN9173 anode. As a result, P-SOEC with LBCN9173 anode demonstrates a top-rank current density of 2.45 A cm^{-2} at 1.3 V and an extremely low polarization resistance of 0.05 Ω cm^2 at 650 °C. This multi-scale, multi-faceted research approach not only discovered a high-performance anode but also proved the robust framework for the machine learning-assisted design of anodes for P-SOECs.

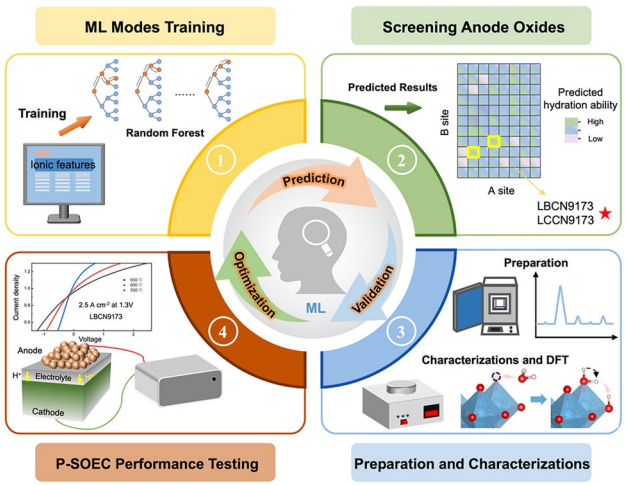

KEYWORDS Machine learning; Proton-conducting solid oxide electrolysis cells; Hydrogen energy; Anode

Fangyuan Zheng and Baoyin Yuan have contributed equally to this work.
✉ Chunmei Tang, tangchunmei554@gzhu.edu.cn; Ning Wang, ningwang@gzhu.edu.cn; Siyu Ye, siyu.ye@gzhu.edu.cn
[1] Huangpu Hydrogen Energy Innovation Center, School of Chemistry and Chemical Engineering, Guangzhou University, Guangzhou 510006, People's Republic of China
[2] School of Mathematics and Information Science, Guangzhou University, Guangzhou 510006, People's Republic of China
[3] School of Materials Science and Engineering, Xihua University, Chengdu 610039, People's Republic of China
[4] Faculty of Engineering, Hokkaido University, N13W8, Kita-Ku, Sapporo 060-8628, Japan

Published online: 23 May 2025

Shanghai Jiao Tong University Press

Springer

1 Introduction

Hydrogen energy has emerged as a promising solution due to its eco-friendliness and high energy density. Current hydrogen energy production technologies operate across various temperature ranges: alkaline water electrolyzers (AWEs) and proton exchange membrane electrolysis cells (PEMECs) at low temperatures (50–90 °C), and oxide-ion conducting and proton-conducting solid oxide electrolysis cells (O-SOECs and P-SOECs) at intermediate-to-high temperatures (400–900 °C) [1]. Among these, AWEs are commercially mature, benefiting from their independence from noble metal catalysts, long-term stability, and low costs. However, they are hindered by high electrode overpotentials, gas crossover, and low current densities (0.2–0.4 A cm^{-2}) [2]. PEMWEs, known for their rapid response and high efficiency, are promising for hydrogen generation but remain reliant on noble metal catalysts. In contrast, solid oxide electrolysis cells (SOECs), particularly P-SOECs, are attracting much attention in renewable energy applications for their high electrolysis efficiency (up to 1 A cm^{-2}) and cost-effectiveness without the need for noble metal catalysts [2–6]. P-SOECs are especially promising for intermediate temperature (400–700 °C) hydrogen production, offering advantages such as lower activation energy and faster proton migration compared to oxide-ion conducting counterparts. This positions P-SOECs as a superior choice for efficient and sustainable hydrogen energy production.

However, the widespread application of P-SOECs still faces numerous challenges, including electrochemical performance optimization of key materials, interface issues, fabrication of large-scale high-performance cells, etc. [2, 6–10]. Developing high-performance anodes for P-SOECs is particularly challenging, which involves the adsorption and dissociation of steam, conduction of oxide ions (O^{2-}) and protons, and the transfer of four electrons [2]. Therefore, achieving efficient synergy between the catalytic activity of steam oxidation and ionic/electronic conductivity is the key for designing high-performance anodes. Traditional Co-based perovskite oxides (such as $La_{1-x}Sr_xCo_{1-y}Fe_yO_{3-\delta}$ (LSCF) and $Ba_{1-x}Sr_xCo_{1-y}Fe_yO_{3-\delta}$ (BSCF)) exhibit good catalytic activity and O^{2-}/e^- conductivity, called mixed ionic-electronic conductors (MIECs) [11, 12]. However, these conventional materials, such as $Ba_{0.5}Sr_{0.5}Co_{0.8}Fe_{0.2}O_{3-\delta}$, exhibit significantly higher TECs (~ 19–21 × 10^{-6} K^{-1}) compared to those (~ 13–16 × 10^{-6} K^{-1}) of new Co/Ni-doped La-based perovskites ($LaCo_{0.2}Cu_{0.2}Fe_{0.2}Ni_{0.2}Cr_{0.2}O_{3-\delta}$), posing substantial challenges to the stability and performance of P-SOCs [13–20]. In order to make proton conduction and other properties side by side, researchers have adopted various strategies, such as elements dopant, the introduction of proton-conducting phase, and design of oxygen deficiency, to develop oxides with both high ionic/electronic conductivity and catalytic activity, and thus enhancing the electrochemical performances of P-SOECs [2, 11]. For instance, the proton rotation energy of $Ba_{0.4}K_{0.1}Sr_{0.5}Co_{0.8}Fe_{0.2}O_{3-\delta}$ was reduced from 0.33 to 0.07 eV by doping BSCF with K [21]. Shao et al. demonstrated that the current density of the P-SOEC increased 3.3 times as the proton-conducting phase $Ba_4Sr_4(Co_{0.8}Fe_{0.2})_4O_{16-\delta}$ introduced to the anode [22]. Ran et al. reported that A-site deficient $Ba_{0.9}Co_{0.4}Fe_{0.4}Zr_{0.1}Y_{0.1}O_{3-\delta}$ facilitates the formation of oxygen vacancies, promoting proton conduction [23]. Although some advances have been made in the development of high-efficiency anodes, it is still far from meeting the requirements of commercial P-SOECs. Therefore, further acceleration of research and development is highly needed to rapidly achieve the synergistic enhancement of catalytic activity and ionic conduction.

With the rapid development of artificial intelligence and the continuous enrichment of material databases, machine learning (ML) has shown significant advantages in materials screening. It can efficiently process massive amounts of data, identify complex structure-performance relationships, and accurately predict the properties of unknown materials. Through continuous learning and optimization, ML models constantly improve prediction accuracy, greatly reducing experimental costs and time, accelerating material development cycles, and achieving special designs. It can simultaneously consider multiple parameters, explore new combinations in a vast material space, and promote interdisciplinary knowledge integration. Several research works have demonstrated the effectiveness of ML in material development [24–26]. For example, Ni et al. used the ML model to predict the area-specific resistance of 6871 different perovskite oxides. Among those, $Sr_{0.9}Cs_{0.1}Co_{0.9}Nb_{0.1}O_3$ oxide was identified and demonstrated exceptional electrochemical activity and low area-specific resistance (ASR) of 0.01 Ω cm^2 at 700 °C [25]. Liu et al. applied high-throughput calculations and data-driven decomposition analysis to predict the

https://doi.org/10.1007/s40820-025-01764-7

thermodynamic stability of 4,455 distinct perovskite oxides. The selected oxide, $PrBaCo_{1.9}Hf_{0.1}O_{5+\delta}$ shows excellent catalytic activity and stability [27]. Meanwhile, they also reported that $BaSn_xCe_{0.8-x}Yb_{0.2}O_{3-\delta}$ electrolyte exhibited superior proton conduction ability compared to the widely used $BaZr_{0.1}Ce_{0.7}Y_{0.1}Yb_{0.1}O_{3-\delta}$ (BZCYYb1711), which is screened by employing high-throughput calculations to predict the vacancy formation energy and hydration reaction energy of 932 electrolytes for P-SOECs [24]. Ye's group also constructed accurate and interpretable ML models with various algorithms to efficiently screen the anode of solid oxide cells, achieving the current density of 0.88 A cm^{-2} at 600 °C with $La_{0.7}Ca_{0.3}Co_{0.8}Ni_{0.2}O_{3-\delta}$ oxide [28, 29].

In the present study, $La_{0.9}Ba_{0.1}Co_{0.7}Ni_{0.3}O_{3-\delta}$ (LBCN9173) and $La_{0.9}Ca_{0.1}Co_{0.7}Ni_{0.3}O_{3-\delta}$ (LCCN9173) were tailored using ML model by predicting the hydration proton concentrations (HPCs) of 3200 distinct perovskite oxides. Through experimental methods, such as thermogravimetric analysis (TG), X-ray photoelectron spectroscopy (XPS), and Fourier transform infrared spectroscopy (FT-IR), combined with density functional theory (DFT) calculations on hydration reaction enthalpy, proton migration energy barrier, and catalytic activity, we comprehensively characterized and analyzed the proton uptake and conduction abilities and catalytic activity of two oxides, further validating the reliability of the constructed ML model. Furthermore, we prepared P-SOECs with LBCN9173 and LCCN9173 anodes and conducted their electrochemical performances. The results showed that P-SOECs with LBCN9173 exhibit excellent water electrolysis performances (current density of 2.45 A cm^{-2} at 1.3 V, polarization resistance of 0.05 Ω cm^2 at 650 °C). Besides, the water oxidation reaction mechanism was elucidated by performing distribution of relaxation times (DRT) and DFT characterizations. Overall, this study has achieved three significant outcomes. First, it reports a novel high-performance anode material that demonstrates excellent electrochemical performance in P-SOECs. Second, it validates the high accuracy and reliability of RF model through comprehensive experimental and DFT calculating verification, establishing a robust approach for materials prediction. Third, it enriches the materials database for P-SOECs through systematic characterization and performance evaluation, providing valuable data resources for accelerating the development of next-generation energy storage and conversion devices.

2 Experimental Section

2.1 Materials Synthesis

$La_{0.9}Ba_{0.1}Co_{0.7}Ni_{0.3}O_3$ (LBCN9173), $La_{0.9}Ca_{0.1}Co_{0.7}Ni_{0.3}O_3$ (LCCN9173), $La_{0.9}Sr_{0.1}Co_{0.7}Ni_{0.3}O_3$ (LSCN9173), and $LaCo_{0.7}Ni_{0.3}O_3$ (LCN73) oxides were synthesized following a sol–gel route method reported elsewhere [29]. First, the $La(NO_3)_2{\cdot}6H_2O$ (Aladdin, 99.99%), $Ba(NO_3)_2$ (Aladdin, 99.99%), $Co(NO_3)_2{\cdot}6H_2O$ (Aladdin, 99.99%), $Ni(NO_3)_2{\cdot}6H_2O$ (Aladdin, 98%), $Sr(NO_3)_2$ (Aladdin, 99.97%), and $CaCO_3$ (Aladdin, 99.99%) were completely dissolved into secondary water, and the citric acid (Aladdin, 99.5%) was added to the obtained solution at 60 °C. Next, the citrate solution was heated with vigorous stirring at a temperature below 85 °C until the gel formed. Instantly, the gel was heated up to 500 °C for 1 h to remove the polymeric chelate. Finally, LBCN9173, LCCN9173, LSCN9173, and LCN73 oxides were obtained by annealing the precursor in a tube furnace at 900 °C for 8 h in the air.

2.2 Preparation of Cells

2.2.1 Single Cell

P-SOEC was fabricated using a solid-state reactive sintering method. Stoichiometric amounts of $BaCO_3$ (Aladdin, 99.8%), ZrO_2 (Aladdin, 99.99%), CeO_2 (Aladdin, 99.9%), Y_2O_3 (Aladdin, 99.999%), and Yb_2O_3 (Aladdin, 99.9%) were mixed by ball milling at 350 r min^{-1} with ethyl alcohol as media for 5 h, followed by drying and sintering at 1100 °C in air for 10 h. The cathode was composed of $BaZr_{0.4}Ce_{0.4}Y_{0.1}Yb_{0.1}O_{3-\delta}$ (BZCYYb4411), NiO (Aladdin, 99%), and starch (Aladdin, 99%) at the weight ratio of 4:6:1. The cathode was pressed into a pellet as a supporter. The electrolyte slurry was then prepared by dispersing in a dispersant (20 wt% polyethyleneimine (MW 28000) dissolved in α-terpineol) and a binder (5 wt% surfactant dissolved in α-terpineol). This slurry was spin-coated onto both surfaces of the cathode pellet to form the electrolyte layers. Subsequently, the cathode and the electrolyte were co-sintered at 1400 °C for 8 h in the air. One side of the disk was polished and painted Ag for the current collection, the other side was screen-printed LBCN9173 or LCCN9173 anode.

2.2.2 Symmetrical Cell

BZCYYb4411 powders with 1 wt.% NiO (Aladdin, 99%) as a sintering aid were dry pressed into pellets using a uniaxial press of 20 MPa for 1 min and then calcined at 1550 °C for 8 h. The anode slurry was prepared by ball milling oxides with α-terpineol in a weight ratio of 1:1.5. The symmetrical cell was fabricated by screen-printed the anodic slurry on both sides of BZCYYb4411 pellet.

2.3 Characterizations

The microstructure of oxides and P-SOECs were measured using a scanning electron microscope (SEM; SU8010, HITACHI) with 3 kV acceleration voltage and field emission transmission electron microscopy (TEM, FEI Talos F200x) with 200 kV acceleration voltage. X-ray powder diffraction (XRD; Rigaku, Ultima IV) was performed by Cu Kα radiation (40 kV, 40 mA) in the 2θ range of 20–80°. The surface element states were identified by X-ray photoelectron spectroscopy (XPS, Thermo Scientific ESCALAB 250XI) under dry condition, which used Al Kα (hv = 1486.6 eV) as the source of X-ray, and the beam spot was 650 μm. The voltage and current are 14.8 kV and 1.6 A, respectively. Peak of C 1*s* (284.8 eV) was used for the peak correction. The oxygen vacancies of oxides were qualitatively identified by electron paramagnetic resonance (EPR, Bruker EPR A300-10/12) at room temperature. Fourier transform infrared spectroscopy (FT-IR) measurements were tested at room temperature and dry air by an equipment (TENSOR II + Hyperion2000). The electrical conductivity of oxide was measured by the DC four-probe method. The thermal expansion coefficient (TEC) were performed using PCY-G-1000 in air with a heating rate of 5 °C min^{-1}. Thermogravimetric (TG) analysis of LBCN9173 and LCCN9173 oxides was performed by a STA6000 thermogravimetric analyzer (PerkinElmer) at a rate of 5 °C min^{-1} under a mixing flow of dry and wet synthetic air (p_{H2O} = 0.02 atm) at 20 sccm. The wet synthetic air was obtained by passing 20% Vol. O_2/80% Vol. Ar mixed gas at total flow of 20 sccm through a water bubbler at room temperature.

For P-SOEC tests, wet hydrogen (3%H_2O/H_2) and wet synthetic air (20% Vol. O_2/80% Vol. Ar) at total flow rate of 15 and 20 sccm were flowed to cathode and anode, respectively. Silver glue (DAD-87, Shanghai, China) was selected as the sealing material to prevent the gas crossover. The P-SOEC single cell is a circular disk with a diameter of approximately 13 mm, and the effective area of the anode is about 0.12 cm^2. The electrochemical impedance spectra (EIS) of the P-SOECs were obtained with a CORRTEST frequency response analyzer implemented with a CORRTEST CS2350M potentiostat using the frequency ranging from 10^5 to 0.1 Hz with an AC amplitude of 30 mV under open circuit voltage (OCV) condition. Moreover, the current–voltage (*I–V*) characteristics were recorded on the same apparatus. Symmetric cell was measured at wet synthetic air with the flow rate of 20 sccm. The DRT converted from impedance spectra was developed by MATLAB.

2.4 DFT Calculation

We employed the Vienna Ab initio Simulation Package (VASP) to perform all DFT calculations with generalized gradient approximation (GGA) using the Perdew–Burke–Ernzerhof (PBE) function. Specifically, projected augmented wave (PAW) potentials were selected to describe the ionic cores. The valence electrons were considered using a plane-wave basis set with a kinetic energy cut-off of 450 eV. Thereafter, geometry optimizations were performed with a force convergence of less than 0.05 eV $Å^{-1}$, where the same convergence was applied to locate the transition states through constrained optimizations (NEB). The oxygen vacancy formation energy (ΔE_{FE}), hydration energy, and proton-conducting barrier energy were investigated under spin-polarized calculations on an LBCN9173/LCCN9173 bulk structure containing 120 atoms. The oxygen vacancy was created by deleting a single oxide ion between Co–Co, Co–Ni, and Ni–Ni, written as Co–$V_O^{\cdot\cdot}$–Co, Co–$V_O^{\cdot\cdot}$–Ni, and Ni–$V_O^{\cdot\cdot}$–Ni. Moreover, oxygen evolution reaction (OER) catalytic activity was calculated on the (001) surface of LBCN9173 and LCCN9173 oxides.

ΔE_{FE} of LBCN9173 and LCCN9173 oxides are calculated according to Eq. 1:

$$\Delta E_{FE} = E_{dehyd} + \frac{1}{2}E_{O_2} - E_{perfect} \quad (1)$$

https://doi.org/10.1007/s40820-025-01764-7

Here, E_{dehyd} and $E_{perfect}$ are the total energy of defective bulk with $V_O^{\cdot\cdot}$ and perfect bulk, respectively. E_{O_2} represents the energy of oxygen molecular in vacuum.

2.5 Machine-Learning Model

Random forest algorithm was employed to predict the HPCs using a comprehensive dataset of 795 perovskite oxides with 66 features, and the data is collected from public references. The model was trained using the "caret" package (short for Classification and Regression Training) in the R platform. Then a tenfold cross-validation resampling procedure was used to improve the model training with the hyperparameter settings of min.node.size = 3, splitrule = beta, and mtry = 24. The model's predictive capability was evaluated through multiple metrics including R^2, RMSE, and MAE. After assessing the predictive performance including accuracy and interpretability, the RF model was used to predict the unknown HPCs of 3200 oxides.

3 Results and Discussion

3.1 Screen the Target Anode Oxides

Figure 1 presents a comprehensive looped workflow for screening and researching high-efficiency anode oxides. This workflow comprises three main parts: ML-guided oxide design, experimental validation, and performance evaluation in P-SOECs, forming an iterative feedback loop. Specifically, ML model is well trained to predict hydrated proton concentration (HPCs) using the collected dataset, which can be used to represent proton conduction ability partly [28–30]. Promising oxide compositions are identified and selected for synthesis and characterization based on the predictions. The experimental results provide crucial feedback, guiding the refinement of the ML models and expanding the dataset. This cycle continuously improves the predictive power of the models while efficiently directing experimental efforts toward the most promising anode oxides for P-SOECs.

The ML model was trained using a dataset comprising the target HPC and 35 descriptors, including temperature, ionic radius, electronegativity, melting point, etc. We employed the random forest (RF) algorithm due to its advantages in handling nonlinear relationships, feature importance

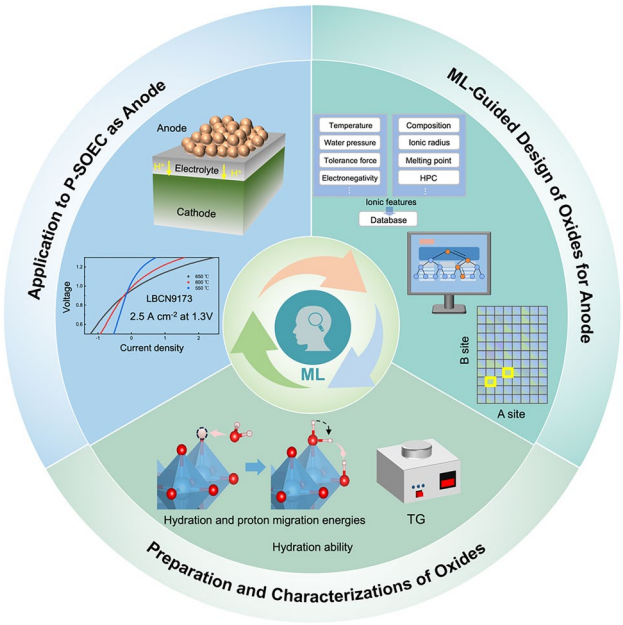

Fig. 1 Comprehensive looped workflow: from ML-guided oxide design to experimental validation and performance evaluation in P-SOECs

ranking, and robustness against overfitting. A tenfold cross-validation approach was implemented during the training process. The distribution of true and predicted HPCs illustrated in Fig. 2a indicates a wide range of values in both the predicted and training datasets, demonstrating the model's capability to handle diverse HPCs. The model demonstrates excellent performance, characterized by low error rates and high predictive accuracy. The distributions of performance metrics with 95% confidence interval (CI) on the basis of the best tuned hyperparameters (mtry = 24, splitrule = beta, and min.node.size = 3) are presented in Fig. 2b–d, including R-squared (0.8967, 95% CI [0.8962, 0.8972]), root mean square Error (RMSE, 0.021 mol $unit^{-1}$, 95% CI [0.0205, 0.0214] mol $unit^{-1}$), and mean absolute error (MAE, 0.0115 mol $unit^{-1}$, 95% CI [0.011, 0.0119] mol $unit^{-1}$). The scatter plot in Fig. 2e visualizes the model's predictive accuracy using these optimized hyperparameters. The model reveals that the ionic radius, melting point, and electronegativity have critical effects on HPCs, as illustrated in Fig. 2f–h. For example, elements with larger ionic radius occupying the A site, combined with cations of smaller ionic radius at the B site, tend to promote hydration reactions in the perovskite oxides. Because the larger A-site elements can provide more space for proton rotation, thereby the enhancing proton

mobility and conduction ability. The smaller the ionic radius of the B-site cation, the shorter the bond length between it and the lattice oxygen. This results in a stronger electrostatic attraction between the two ions. This stronger bonding makes it easier for the lattice oxygen to accept protons [11]. Overall, the high-accuracy and explainable RF model is well-constructed and used for the further prediction.

The predicted oxides are divided into four categories based on whether the perovskite structure oxides (ABO_3) contain Al, Ba, Ca, or Mg at the A-site. Figure 2i shows the violin plots with overlaid box plots for HPCs of these oxides. Each dopant is represented by a differently colored violin shape, providing a visual representation of the data distribution. Both Ba-(0.042 mol unit^{-1}) and Ca-(0.042 mol unit^{-1}) containing oxides show higher median predicted HPCs compared to Al-(0.038 mol unit^{-1}) and Mg-(0.041 mol unit^{-1}) containing oxides, and their distributions extend to higher values, indicating the potential for high HPCs. The box plots within these violins also suggest a wider interquartile range for Ba-containing oxides compared to Ca-containing oxides, further emphasizing the high-HPCs possibility of Ba-containing oxides. The results indicate that Ba and Ca at the A-site are conducive to proton incorporation, making them ideal proton conduction. Based on our previous report, oxides with $Co_{0.7}Ni_{0.3}$ at B-site show promising proton conductivity and water oxidation catalytic ability [29]. Accordingly, (La,Ba)$(Co_{0.7}Ni_{0.3})O_3$ and (La,Ca)$(Co_{0.7}Ni_{0.3})O_3$ oxides were selected to be the target oxides. Further, HPCs of $(La_{1-x}Ba_x)(Co_{0.7}Ni_{0.3})O_3$ and $(La_{1-x}Ca_x)(Co_{0.7}Ni_{0.3})O_3$ oxides ($x = 0.1, 0.2, 0.3, 0.4$) are predicted and shown in Fig. 2j. The results manifest that $(La_{0.9}Ba_{0.1})(Co_{0.7}Ni_{0.3})O_3$ (LBCN9173) and $(La_{0.9}Ca_{0.1})(Co_{0.7}Ni_{0.3})O_3$ (LCCN9173) oxides show the highest HPCs at each oxide family. Finally, LBCN9173 and LCCN9173 oxides are selected for further preparation, characterizations and application.

3.2 Phase Structure and Microstructure of the Screened Oxides

X-ray diffraction (XRD) patterns (Figs. 3a, b and S1a) suggest that LBCN9173 and LCCN9173 oxides display a pure perovskite structure without observable secondary phase, corresponds well with the PDF card of $LaCoO_{3-\delta}$ ($R\bar{3}c$, PDF # 48-0123). The (110) peak at 32°–34° of LBCN9173 oxide (Fig. S1b) shifts to lower angle compared to that of LCCN9173 oxide, indicating an expansion of LBCN9173 oxide lattice. The XRD Rietveld refinements were conducted with rhombohedral ($R\bar{3}c$) $LaCoO_{3-\delta}$-derived phase structure, shown in Figs. 3e and S2. The results are reliable with small R_p (2.76% and 3.87%), R_{wp} (3.66% and 4.88%) and R_{exp} (0.85% and 1.01%) for LBCN9173 and LCCN9173 oxides. The calculated lattice parameters of LBCN9173 (5.4547 Å) oxide is larger than that of LCCN9173 (5.4476 Å) (Table S1) oxide. High resolution transmission electron microscope (HR-TEM) images also suggest the expanded lattice of LBCN9173 oxide with the (110) interplanar spacing of 0.284 nm, higher than that of LCCN9173 oxide (0.275 nm) (Fig. 3c, d). These phenomena are reasonable due to the larger ionic radius of Ba^{2+} (0.135 nm) than Ca^{2+} (0.100 nm). Figure 3f, g shows the elemental distribution of LBCN9173 and LCCN9173 oxides, indicating the homogeneous distribution of elements La, Ba/Ca, Co, Ni, and O without any element segregation, and it also suggests that Ba and Ca have been successfully incorporated into the LBCN9173 and LCCN9173 oxides lattice, respectively.

3.3 Proton Uptake and Conduction Ability of the Screened Oxides

Figures 4a and S3 show the TG curves of LBCN9173 and LCCN9173 oxides under dry and wet ($p_{H2O} = 0.02$ atm) air at 50–800 °C. A distinct weight gap (defined as ΔW) appears between the two curves due to the hydration reaction as described in Kröger–Vink notation (Eq. 2) [44]. For example, the ΔW for LBCN9173 and LCCN9173 oxides is 0.270% and 0.197% at 500 °C, respectively. The measured HPCs of LBCN9173 and LCCN9173 oxides can be quantified by using the ΔW, which are the twice as the absorbed water molar mass (HPC $= 2 \times \Delta n$ (H_2O)/Δn (oxide)), shown in Figs. 4b and S4 [12]. The measured HPCs of LBCN9173 oxide are 0.060, 0.052, and 0.041 mol unit^{-1} at 450, 500, and 550 °C, respectively, higher than those of LCCN9173 oxide (0.050, 0.048, and 0.039 mol unit^{-1}). Moreover, the experimental results match well with the predicted HPCs (Fig. 4c). For instance, the measured *vs.* predicted HPCs of LBCN9173 oxide are 0.052 *vs.* 0.049 mol unit^{-1} and

https://doi.org/10.1007/s40820-025-01764-7

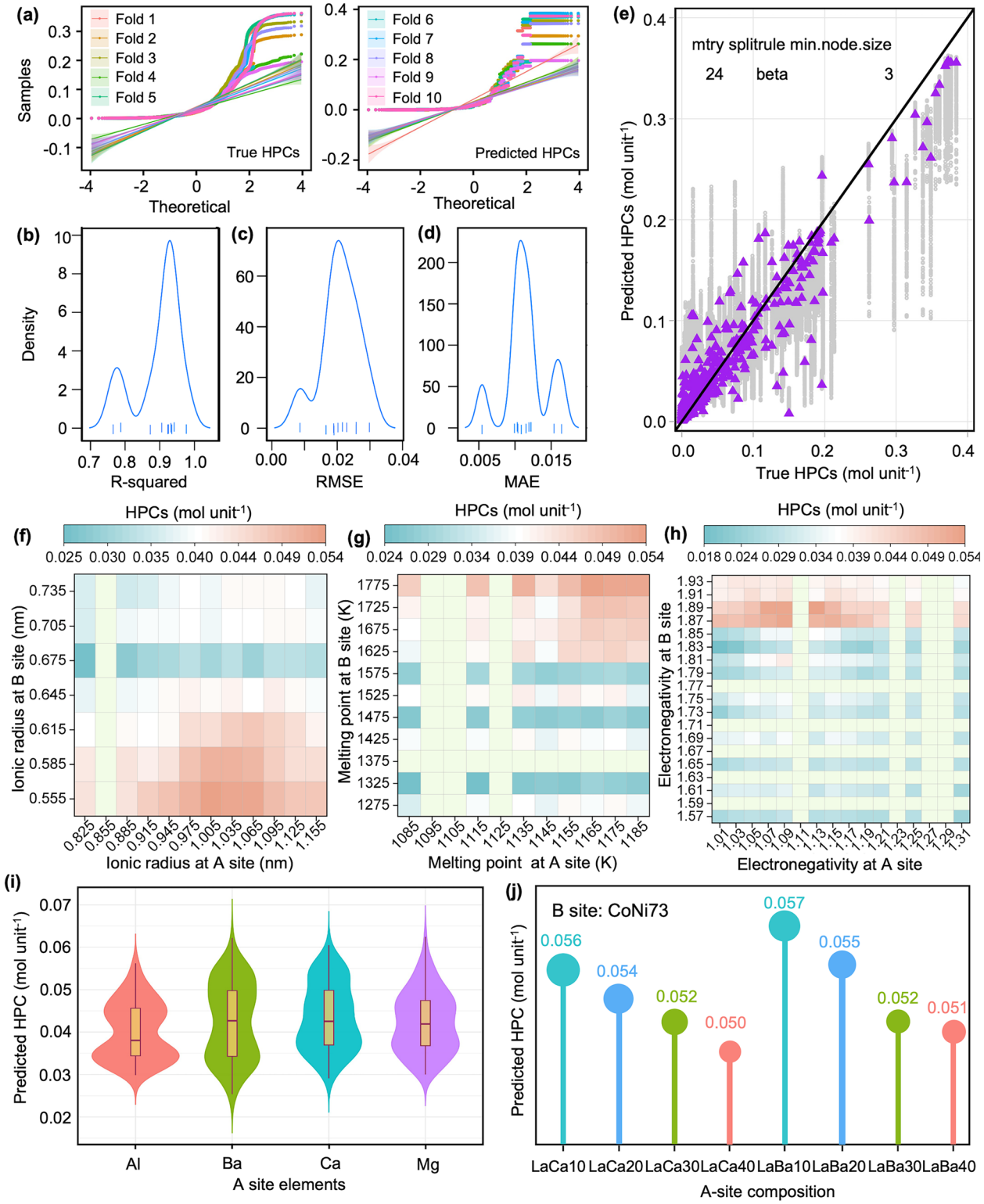

Fig. 2 Performance evaluation of ML model and predicting results. **a** Distribution of true and predicted HPCs across tenfold cross-validation. Distribution of **b** R-squared, **c** Root Mean Square Error (RMSE) and **d** Mean Absolute Error (MAE). **e** Scatter plot of true vs. predicted HPCs during the ML training process. **f–h** Correlations between ionic radius, electronegativity, and melting point of A and B site elements with predicted HPCs. **i** Violin plots with overlaid box plots for predicted HPCs of Al-, Ba-, Ca-, or Mg-containing oxides at A site. **j** Predicted HPCs of $(La_{1-x}Ba_x)(Co_{0.7}Ni_{0.3})O_3$ and $(La_{1-x}Ca_x)(Co_{0.7}Ni_{0.3})O_3$ oxides ($x = 0.1, 0.2, 0.3, 0.4$)

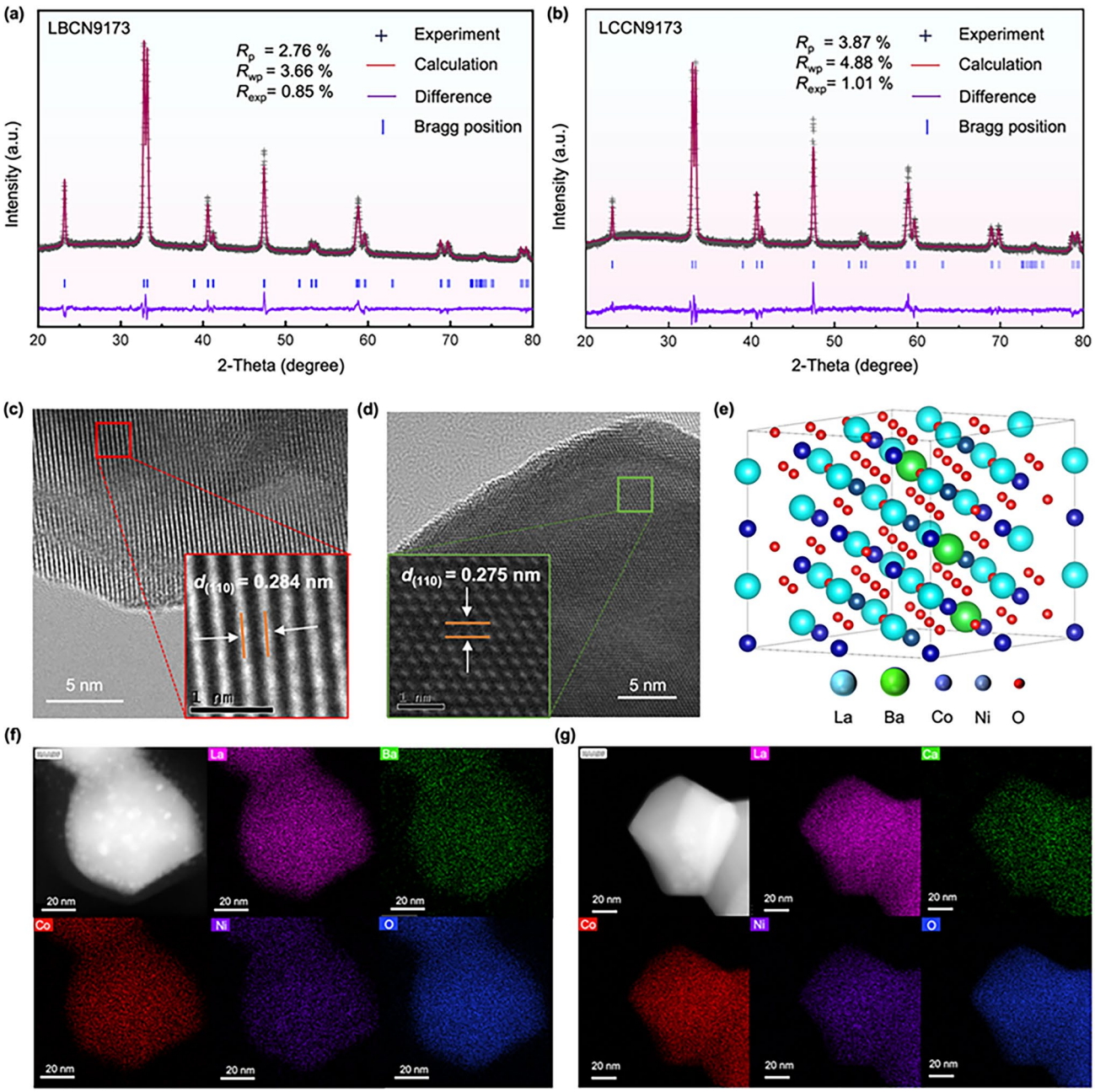

Fig. 3 Phase structure and microstructure of LBCN9173 and LCCN9173 oxides. **a, b** XRD refinement results, **c, d** HR-TEM images, and **f, g** STEM-EDX mapping images for LBCN9173 and LCCN9173 oxides. **e** Phase structure of LBCN9173 oxide

0.041 *vs.* 0.046 mol unit^{-1} at 500 and 550 °C, respectively. The results suggest that the used ML model is highly accurate and reliable. Furthermore, HPCs of LBCN9173 and LCCN9173 oxides as function of p_{H2O} (0–0.05 atm) and temperatures (50–800 °C) are further predicted, shown in Fig. S5, offering a guideline for the application of these oxides in wide ranges of steam pressure and temperature. The HPCs of LBCN9173 oxide are higher than 0.04 mol unit^{-1} above 500 °C, which are superior to many other reported anodes (Fig. 4f), such as $BaCo_{0.4}Fe_{0.4}Zr_{0.1}Y_{0.1}O_{3-\delta}$ (0.019 mol unit^{-1}) [38], $PrBa_{0.5}Sr_{0.5}Co_{1.5}Fe_{0.5}O_{5+\delta}$ (0.02 mol unit^{-1}) [35], enabling the matchable proton conduction

https://doi.org/10.1007/s40820-025-01764-7

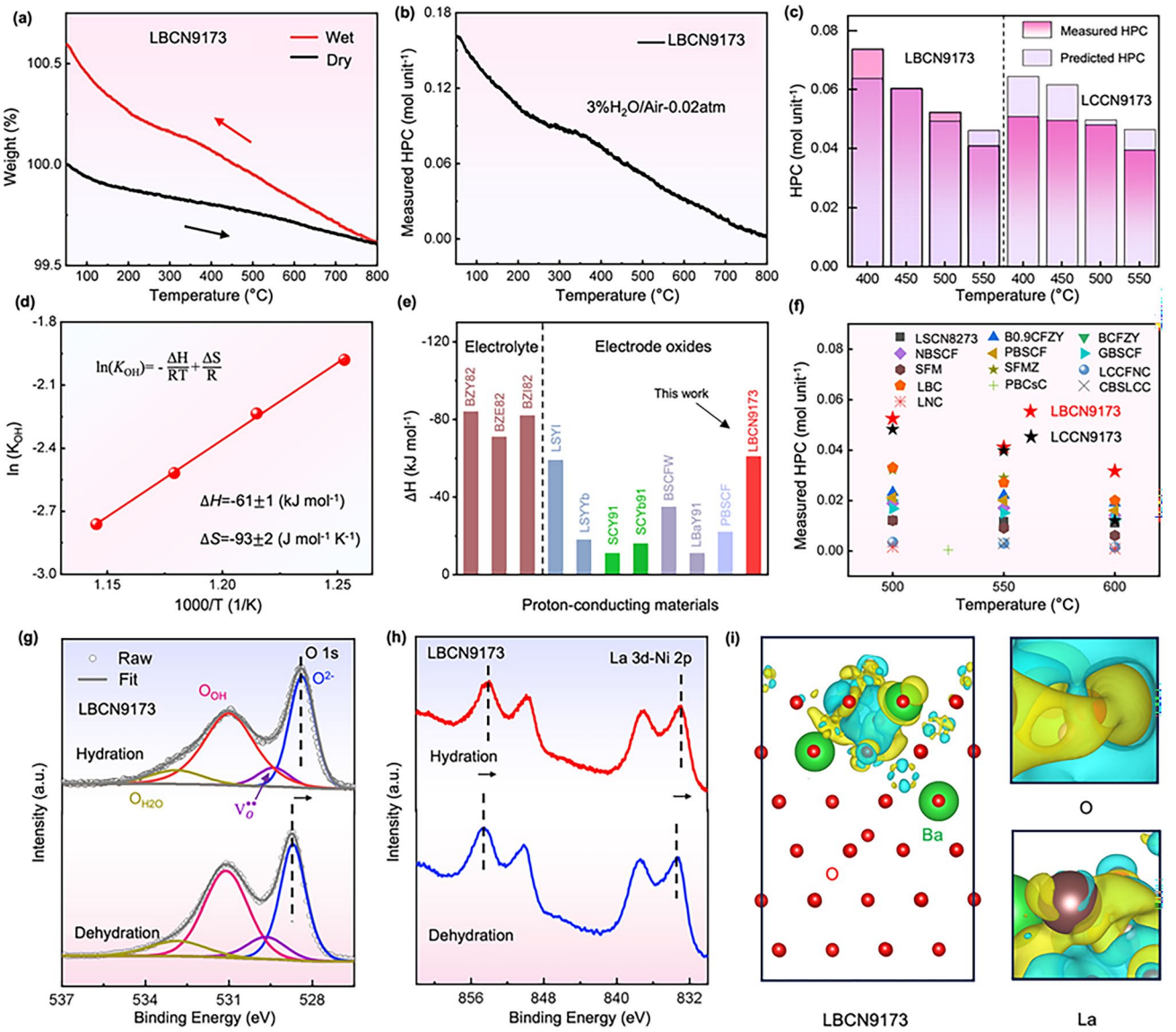

Fig. 4 **a** TG curves of LBCN9173 oxide under dry and wet air (p_{H2O} = 0.02 atm) at 50–800 °C. **b** Measured HPCs of LBCN9173 oxide. **c** Comparison of measured and predicted HPCs at 400, 450, 500, and 550 °C for LBCN9173 and LCCN9173 oxides. **d** Arrhenius plot showing the equilibrium constant of hydration reaction as a function of temperature for LBCN9173 oxide. **e** ΔH of LBCN9173 oxide and reported oxides. **f** Summary of HPCs for LBCN9173, LCCN9173, and reported oxides. XPS spectra of **g** O 1*s* and **h** La 3*d*-Ni 2*p* for hydrated and dehydrated LBCN9173 samples. **i** The differential charge density of hydrated LBCN9173 oxide with two protons. Abbreviations: BZY82 = $BaZr_{0.8}Y_{0.2}O_{3-\delta}$ [31], BZI82 = $BaZr_{0.8}In_{0.2}O_{3-\delta}$, BZE82 = $BaZr_{0.8}Er_{0.2}O_{3-\delta}$, LSYI = $La_{0.9}Sr_{0.1}Y_{0.8}In_{0.2}O_{3-\delta}$, SCY91 = $SrCe_{0.9}Y_{0.1}O_{3-\delta}$, SCYb91 = $SrCe_{0.9}Yb_{0.1}O_{3-\delta}$, LSYYb = $La_{0.9}Sr_{0.1}Y_{0.8}Yb_{0.2}O_{3-\delta}$ [32], BSCFW = $Ba_{0.5}Sr_{0.5}(Co_{0.7}Fe_{0.3})_{0.6875}W_{0.3125}O_{3-\delta}$ [33], LBYb91 = $La_{0.9}Ba_{0.1}YbO_{3-\delta}$ [34], PBSCF = $PrBa_{0.5}Sr_{0.5}Co_{1.5}Fe_{0.5}O_{5+\delta}$ [35], SFM = $Sr_2Fe_{1.5}Mo_{0.5}O_{6-\delta}$, SFMZ = $Sr_2Fe_{1.5}Mo_{0.4}Zr_{0.1}O_{6-\delta}$ [36], GBSCF = $GdBa_{0.5}Sr_{0.5}Co_{1.5}Fe_{0.5}O_{5+\delta}$, NBSCF = $NdBa_{0.5}Sr_{0.5}Co_{1.5}Fe_{0.5}O_{5+\delta}$ [37], BCFZY = $BaCo_{0.4}Fe_{0.4}Zr_{0.1}Y_{0.1}O_{3-\delta}$ [38], B0.9CFZY = $Ba_{0.9}Co_{0.4}Fe_{0.4}Zr_{0.1}Y_{0.1}O_{3-\delta}$ [23], LSCN8273 = $La_{0.8}Sr_{0.2}Co_{0.7}Ni_{0.3}O_{3-\delta}$ [39], LBC = $La_{0.9}Ba_{0.1}CoO_{3-\delta}$ [40], LCCFNC = $La(Co_{0.2}Cu_{0.2}Fe_{0.2}Ni_{0.2}Cr_{0.2})O_{3-\delta}$ [14], CBSLCC = $Ce_{0.2}Ba_{0.2}Sr_{0.2}La_{0.2}Ca_{0.2}CoO_{3-\delta}$ [41], PBCsC = $PrBa_{0.875}Cs_{0.125}Co_2O_{5+\delta}$ [42], LNC = $La_2Ni_{0.9}Co_{0.1}O_{4+\delta}$ [43]

in-between the electrolyte and the anode during steam electrolysis [14, 35–43].

The excellent hydration ability of LBCN9173 oxide drives us to understand its thermodynamics. The equilibrium constant of hydration (K_{OH}), hydration enthalpy (ΔH) and hydration entropy (ΔS) are calculated. Note that the sum of concentration of $V_O^{\cdot\cdot}$, $OH_O^{\cdot}$ and $O_O^{\times}$ is 3 in ABO_3 perovskite oxides. Combined with the known parameters, K_{OH} expressed as Eq. 3 can be calculated [35]. Shown in Fig. 4d is the Arrhenius plot for K_{OH} as function of

temperature. Accordingly, ΔH and ΔS of the oxide are -61 ± 1 kJ mol^{-1}and -93 ± 2 J mol^{-1} K^{-1} (Fig. 4d) based on the Van't Höff equation (Eq. 4) [33]. The more negative values of ΔH indicate that hydration reaction is more favorable. ΔH of LBCN9173 oxide is lower than the well-known anodes, such as $Ba_{0.5}Sr_{0.5}(Co_{0.7}Fe_{0.3})_{0.6875}W_{0.3125}O_{3-\delta}$ ($-$ 35 kJ mol^{-1}) [33], $PrBa_{0.5}Sr_{0.5}Co_{1.5}Fe_{0.5}O_{5+\delta}$ ($-$ 22 kJ mol^{-1} at 400 °C) [35], and even can be comparable to these of the electrolytes (Fig. 4e) [31–35]. Overall, LBCN9173 selected through the ML model exhibits the excellent hydration ability.

$$O_O^{\times} + V_O^{\cdot\cdot} + H_2O \rightarrow 2OH_O^{\cdot} \quad (2)$$

$$K_{OH} = \frac{\left[OH_O^{\cdot}\right]^2}{p_{H2O}\left[V_O^{\cdot\cdot}\right]\left[O_O^{x}\right]} \quad (3)$$

$$\ln\left(K_{OH}\right) = -\frac{\Delta H}{RT} + \frac{\Delta S}{R} \quad (4)$$

where $V_O^{\cdot\cdot}$, $OH_O^{\cdot}$ and $O_O^{\times}$ represent oxygen vacancies, proton defect, and lattice oxygen in Eqs. 2 and 3, respectively. R and T represent the universal gas constant and absolute temperature in Eq. 4.

In order to characterize the proton defects, LBCN9173 oxide was treated at 500 °C under dry and wet air for 3 h, respectively, called dehydrated and hydrated LBCN9173 samples, then immediately measured using the XPS and FT-IR. FT-IR spectra of hydrated LBCN9173 oxide present a prominent hydroxyl (–OH) peak at approximately 3500 cm^{-1} compared to the dehydrated one (Fig. S6) [45]. This further confirms that hydration reaction occurs in LBCN9173 oxide. The high-resolution narrow XPS spectra of O 1*s*, Co 2*p*, La 3*d*-Ni 2*p*, and Ba 3*d* for the hydrated and dehydrated LBCN9173 samples are present in Figs. 4g, h and S7. The O 1*s* XPS spectra are deconvoluted into four peaks at approximately 528.3, 529.3, 530.9, and 532.9 eV, corresponding to lattice oxygen (O^{2-}), chemisorbed oxygen at oxygen vacancy ($V_O^{\cdot\cdot}$) site, hydroxylated oxygen species (O_{OH}), and absorbed surface water (O_{H2O}), respectively [46]. The fitting results are shown in Table S2. The ratio of $V_O^{\cdot\cdot}$/O^{2-} decreases from 27 to 21%, and the O_{OH} increases from 44 to 48% after hydration, indicating the occurrence of proton defects in LBCN9173 oxide (Fig. S8) [44]. Moreover, the O 1*s* XPS fitting results revealed that LBCN9173 exhibits a higher $V_O^{\cdot\cdot}$ concentration than that of LCCN9173 (Fig. S8 and Table S2), which is also evidenced by the stronger EPR signal intensity of LBCN9173 compared to that of LCCN9173 (Fig. S9), indicating a higher $V_O^{\cdot\cdot}$ concentration [47]. As compared with $LaCo_{0.7}Ni_{0.3}O_3$ (LCN73) with rhombohedral phase structure (Fig. S10), LBCN9173 and LCCN9173 possess more oxygen vacancy due to the acceptor doping at A-site [21, 48]. When acceptor doping is introduced at the A-site, it fundamentally leads to either an increase in hole conductivity or a rise in $V_O^{\cdot\cdot}$ concentration. The electrical conductivity of LBCN9173 ranges from 120 to 304 S cm^{-1} at 350–750 °C, lowering than those of $LaCoO_3$ (430–675 S cm^{-1}) and $La_{0.95}Ba_{0.05}CoO_3$ (300–360 S cm^{-1}), shown in Fig. S11. The above results indicate that LBCN9173 tends to increase the $V_O^{\cdot\cdot}$ concentration rather than the hole conductivity to maintain charge neutrality as Ba doped at A-site.

In addition, it is evident that the charge accumulation around lattice oxygen attributes to the excellent ability of LBCN9173 oxide (Fig. 4i), making the proton a more favorable attachment. In Fig. 4i, the yellow region represents charge accumulation, whereas the blue region represents charge reduction. There is apparent charge accumulation around lattice oxygen and La, which corresponds well with the negative shift of O 1*s* and La 3*d* spectra (Fig. 4g, h). As for LCCN9173 oxide, peak shift of all elements and charge accumulation cannot be observed during the hydration reaction (Figs. S12 and S13), ascribing the smaller ionic radius of Ca^{2+} (0.100 nm) than that of Ba^{2+} (0.135 nm) [47, 49, 50].

3.4 DFT Calculations on Proton-Conducting Ability and Catalytic Activity

To further investigate the proton conduction ability of LBCN9173 and LCCN9173 oxides, we performed DFT calculations on their $V_O^{\cdot\cdot}$ formation energies (ΔE_{FE}), hydration energy ($\Delta E_{hydration}$) and proton-conducting energy barriers. Structure models containing 120 atoms were constructed, as illustrated in Figs. 3e and S2. The $V_O^{\cdot\cdot}$ was created by extracting lattice oxygen neighboring the La–La, Ba/Ca–La, and Ba/Ca–Ba/Ca sites from the perfect lattice (Figs. 5a, b and S14, S15). The calculated ΔE_{FE} for LBCN9173 oxide are 2.23 eV at the La–La site, 1.99 eV at the Ba–La site, and 1.67 eV at the Ba–Ba site. These values are all lower than their counterparts in LCCN9173 oxide (Fig. 5c and Table S3), indicating that LBCN9173 oxide is more favorable for the formation of $V_O^{\cdot\cdot}$. These values are all lower than

https://doi.org/10.1007/s40820-025-01764-7

those of LCCN9173 oxide (Fig. 5c and Table S3), indicating that LBCN9173 oxide is more favorable for the formation of $V_O^{\cdot\cdot}$. The calculated results are in consistent with the experimental results (Figs. S8 and S9), that is the lower ΔE_{FE} indicates the higher $V_O^{\cdot\cdot}$ concentration. This enhanced propensity for $V_O^{\cdot\cdot}$ formation in LBCN9173 can be attributed to the larger ionic radius of Ba^{2+} (0.135 nm) compared to Ca^{2+} (0.100 nm) [21]. Because the presence of larger Ba^{2+} ions induces several structural and electronic effects, such as increased steric hindrance, enhanced lattice relaxation and stress release, increased bond length and reduced bond energy, and changes in charge distribution and electronic structure [21, 51, 52]. These factors collectively contribute to the lower $V_O^{\cdot\cdot}$ formation energy, and thus the higher $V_O^{\cdot\cdot}$ concentration in LBCN9173 oxide (Figs. 5c and S8, S9, and Table S3).

To model the hydration process, a proton defect and a proton split from water are incorporated into the formed $V_O^{\cdot\cdot}$, with the latter bonding to a lattice oxygen (Fig. 5a). Accordingly, $\Delta E_{hydration}$ can be calculated based on Eq. 5 [28]. The $\Delta E_{hydration}$ calculating results for LBCN9173 and LCCN9173 oxides with three types $V_O^{\cdot\cdot}$ are shown in Figs. 5b and S14, S15, and Table S3. $\Delta E_{hydration}$ of LBCN9173 oxide is consistently lower than that of LCCN9173 oxide (− 2.30 eV at Ba–Ba site and − 1.02 eV at Ca–Ca site), demonstrating the superior hydration capability of LBCN9173 to LCCN9173 oxides. The results correspond with both experimental and predicted HPCs mentioned above.

$$\Delta E_{hydration} = E_{hyd} - E_{dehyd} - E_{H_2O} \quad (5)$$

where $\Delta E_{hydration}$ is the hydration energy, E_{hyd} represent the total energy of the defective bulk with protons after the hydration reaction, E_{dehyd} is the total energy of the defective bulk with $V_O^{\cdot\cdot}$, and E_{H_2O} is the energy of a single water molecule in a vacuum.

Given that the Ba–Ba (LBCN9173) and Ca–Ca (LCCN9173) sites exhibit the lowest $\Delta E_{hydration}$, we focused our subsequent analysis on this hydrated state to determine the proton-conducting energy barrier. The proton conduction mechanism involves processes such as proton rotation and hopping (Fig. 5d) [11]. For LBCN9173 and LCCN9173, the proton-conducting energy barriers from O1 to O2 are 0.43 and 0.57 eV, respectively, while the barriers from O2 to O3 are 0.74 and 0.79 eV, respectively (Figs. 5f and S16, and Table S4). These results clearly demonstrate that LBCN9173 exhibits consistently lower proton migration energy barriers along the same migration path compared to LCCN9173, confirming its superior proton conduction ability. Evidently, the lower energy barrier observed for the O_1 to O_2 migration path suggests that proton migration is more favorable along this route [29]. The initials states (IS), transition state (TS), final states (FS), and the complete paths are presented in Figs. 5e and S17, S18. Moreover, this migration energy barrier (0.43 eV) is comparably to some previously reported proton-conducting oxide (e.g., BSCF (0.55 eV) [21], $La_{0.5}Sr_{0.5}Fe_{0.9}Sb_{0.1}O_{3-\delta}$ (0.79 eV) [53], $La_{0.5}Sr_{0.5}MnO_{3-\delta}$ (0.684 eV)) [54], $BaCeO_{3-\delta}$ (0.46 eV) [55], $BaZr_{0.85}Y_{0.15}O_{3-\delta}$ (0.43 eV), and $BaCe_{0.85}Y_{0.15}O_{3-\delta}$ (0.59 eV) [31].

Besides proton conduction ability of LBCN9173 and LCCN9173 oxides, Gibbs free energies for oxygen evolution reaction (OER) processes, which is also a crucial property of anode, were calculated on (001) surfaces of LBCN9173 and LCCN9173 oxides with 120 atoms fixed at the bottom (Figs. 3e and S2). Shown in Figs. 6a and S19, OER processes are divided into several steps, i.e., 1) the initial state (IS) corresponds to the reduction of adsorbed oxygen species ($2O^*$), 2) the transition states (TS) involve the adsorption of the oxygen molecule (O_2^*), and 3) the final state (FS) represents the formation of molecular oxygen (O_2) [28]. The Gibbs free energy changes (ΔG) of each step is located at the center of Fig. 6a. The OER reaction energy barriers are 3.31 eV and 3.49 eV, respectively, for LBCN9173 and LCCN9173 oxides, indicating the higher OER catalytic activity of LBCN9173 oxide (Fig. 6a). Overall, LBCN9173 oxide shows superior proton-conducting ability and OER catalytic activity to LCCN9173 oxide.

Long-term stability is a critical factor for the anode of P-SOEC. Therefore, the tolerance to steam and CO_2 for LBCN9173 oxide were tested in wet air ($p_{H2O} = 0.02$ atm) and mixture gas (air with 20% CO_2), respectively, at 600 °C for 100 h. The XRD patterns of LBCN9173 after these treatments show a pure phase without any change as compared to that of before treatment (Fig. 6b). In addition, the stability of the BZCYYb4411-symmetric cell with LBCN9173 electrode was conducted at 550 °C for 100 h by measuring EIS, shown in Fig. 6d. The ASR is stable at 0.684 Ω cm^2, indicating the good stability and catalytic activity of LBCN9173 as electrode.

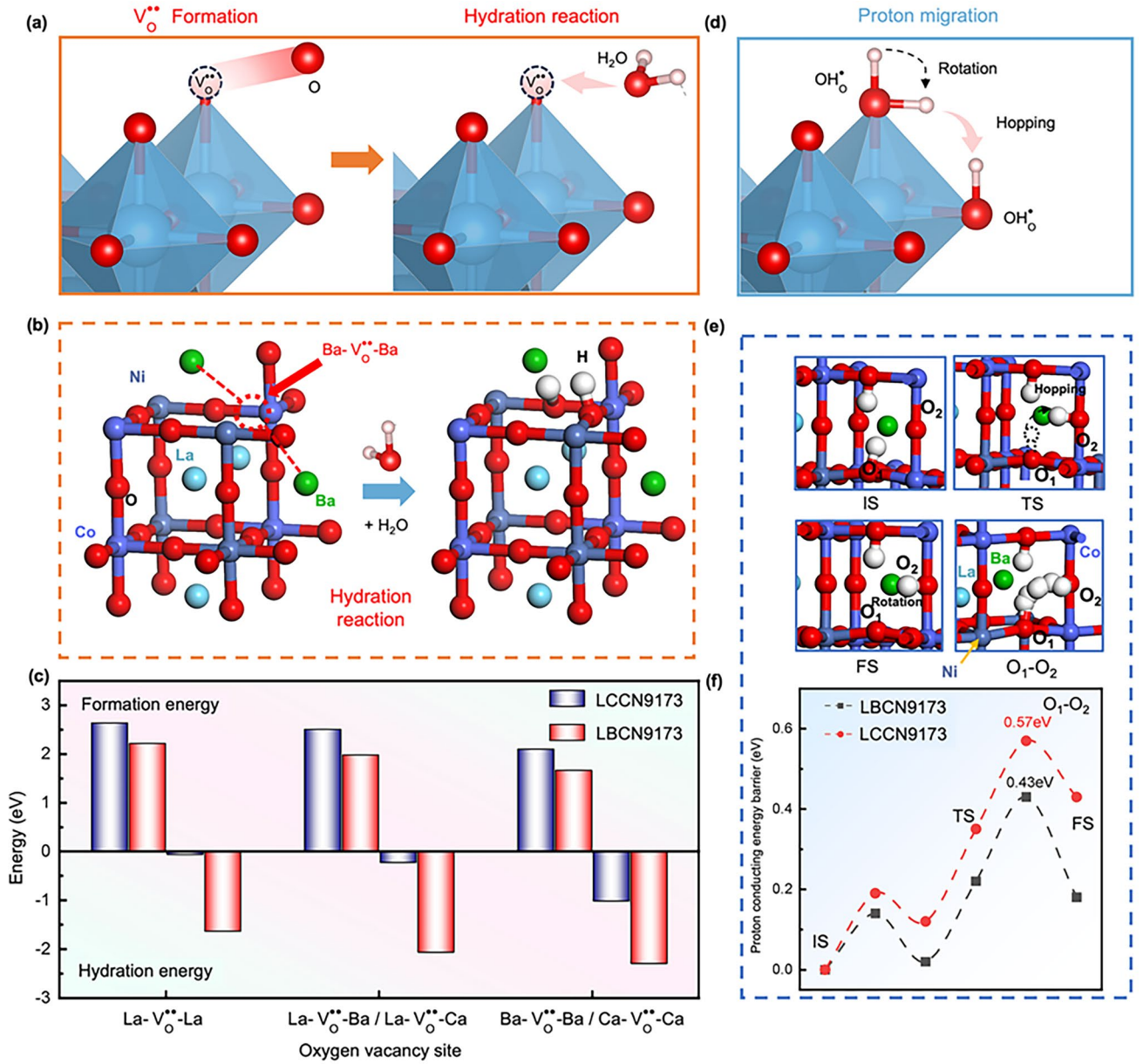

Fig. 5 Scheme of **a** $V_O^{\cdot\cdot}$ formation, hydration reaction and **d** proton rotation / hopping in perovskite oxides. **b** Models for hydration reaction process of LBCN9173 oxide. **c** Calculated $V_O^{\cdot\cdot}$ formation energy and hydration energy of LBCN9173 and LCCN9173 oxides with $V_O^{\cdot\cdot}$ at La-La site, Ba/Ca-La site, and Ba/Ca-Ba/Ca site. **e** Models (IS, TS, and FS) for proton transferring from O_1 to O_2 site. **f** Proton-conducting energy barriers from O_1 to O_2 site in LBCN9173 and LCCN9173 oxides

3.5 Application to Anodes of P-SOECs

LBCN9173 and LCCN9173 oxides were employed as anodes of P-SOECs for single-cell testing. XRD patterns (Fig. S20) of the cell components confirm the presence of BZCYYb4411 phase in the electrolyte layer and the presence of NiO-BZCYYb4411 phases in the cathode support, without the impurity phase. The cross-section SEM images of both cells displayed in Figs. S21a and S22a reveal a typical sandwich structure, which is configured with the identical BZCYYb4411 electrolyte (~ 11–13 μm) layer, a porous Ni-BZCYYb4411 cathode support and a porous anode layer (Figs. S21b, c and S22b, c). Figures S21b and S22b provide a magnified view of the interface between the electrolyte and anode, demonstrating the strong bonding between these two layers, which can be attributed to

 https://doi.org/10.1007/s40820-025-01764-7

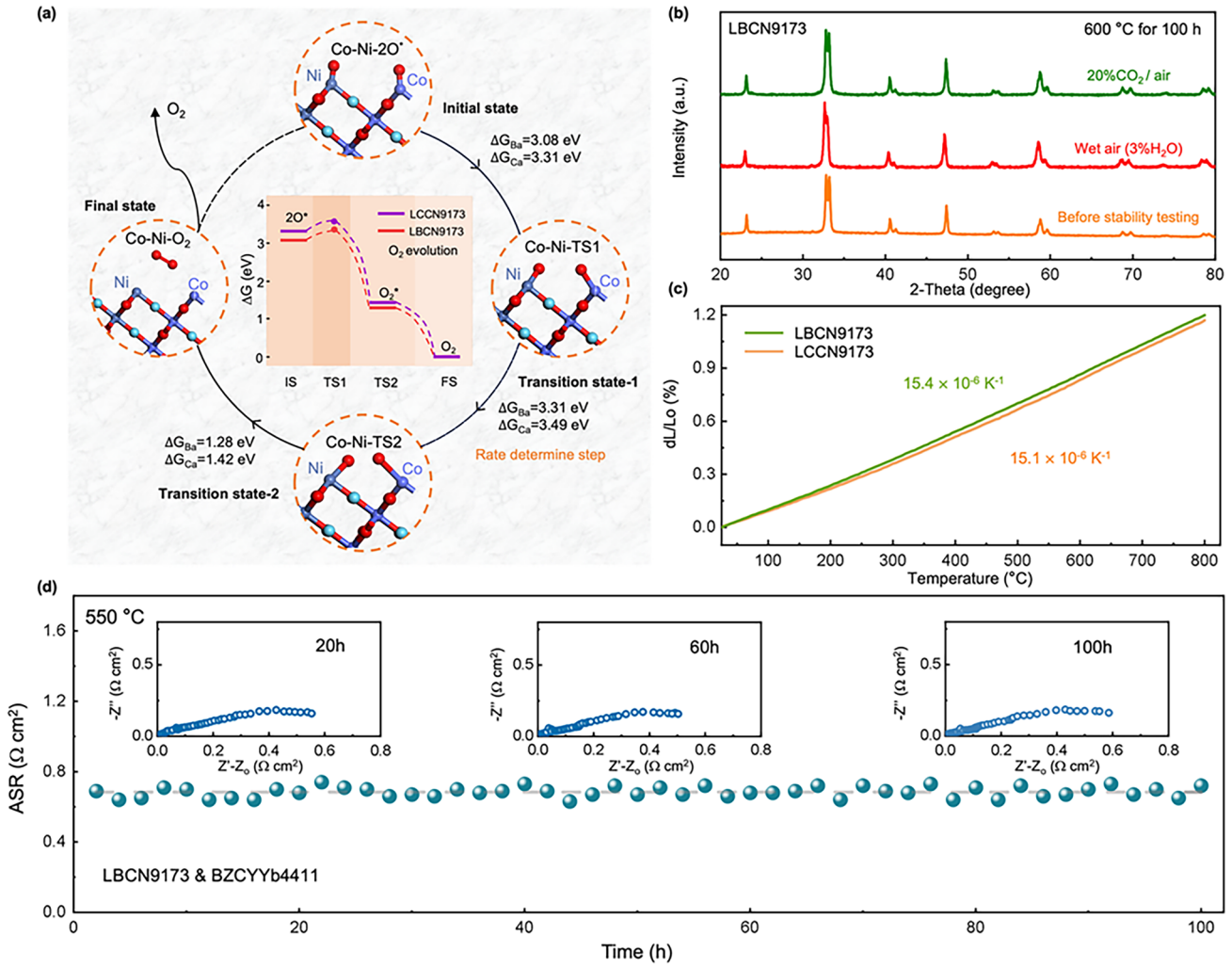

Fig. 6 **a** Illustration of OER reaction states (IS, TS1, TS2, FS) and the Gibbs free energy changes profiles of OER at Co–Ni site on (001) surface for LBCN9173 and LCCN9173 oxides. **b** XRD patterns of LBCN9173 before and after exposing to wet air and mixture gas (air with 20% CO_2), respectively, for 100 h at 600 °C. **c** TEC curves of LBCN9173 and LCCN9173 oxides. **d** ASR stability of the LBCN9173 in wet air at 550 °C

the lower TECs of LBCN9173 (15.4×10^{-6} K^{-1}) and LCCN9173 (15.1×10^{-6} K^{-1}) oxides (Fig. 6c). These TEC values are lower than the well-known electrode, such as $Ba_{0.5}Sr_{0.5}Co_{0.8}Fe_{0.2}O_{3-\delta}$ (BSCF, 19.7×10^{-6} K^{-1}), $BaCo_{0.4}Fe_{0.4}Zr_{0.1}Y_{0.1}O_{3-\delta}$ (BCFZY, 20.4×10^{-6} K^{-1}), and $PrNi_{0.5}Co_{0.5}O_{3-\delta}$ (PNC, 19.2×10^{-6} K^{-1}), and even can be comparable with the Co-free oxides, such as $La_{0.6}Sr_{0.4}Fe_{0.8}Ni_{0.2}O_{3-\delta}$ (13.7×10^{-6} K^{-1}) and $Pr_{0.5}Sr_{0.5}Fe_{0.8}Cu_{0.2}O_{3-\delta}$ (16.4×10^{-6} K^{-1}), listed in Table S5. Furthermore, when the anodes and BZCYYb4411 composite (with a mass ratio of 1:1) were calcined at 650 °C in air for 50 h, the XRD patterns revealed that the individual phases were maintained without the appearance of additional peaks (Fig. S23). This confirms the excellent stability of the constructed cell and the electrolyte/electrode interfaces, as well as the absence of any undesirable chemical reactions.

The electrochemical performances were tested at temperatures ranging from 550 to 650 °C with wet synthetic air (20% Vol. O_2 and 80% Vol. Ar) supplied into the anode and 3% H_2O/97% H_2 fed to the cathode. Figure 7a, b illustrates the *I–V* curves of P-SOECs using LBCN9173 and LCCN9173 anodes. P-SOEC with LBCN9173 anode exhibits the current densities of 0.73, 1.58, and 2.45 A cm^{-2} at 1.3 V at 550, 600, and 650 °C, respectively, while those of LCCN9173 cell demonstrated lower values of 0.60, 1.10, and 1.48 A cm^{-2} at 1.3 V. The current densities of LBCN9173 cell are 22%,

44%, and 66% higher than those of LCCN9173 cell at each above-mentioned temperatures (Fig. 7c), attributing to the higher catalytic activity and stronger proton uptake and conduction ability of LBCN9173 oxide as earlier discussed. The P-SOEC with LBCN9173 anode can stably operate for 40 h without obvious degradation at a constant current density of 0.5 A cm^{-2} and 550 °C (Fig. S24). Meanwhile, the *I–V* curves of P-SOEC with LBCN9173 anode were tested by applying the wet gas with hydrogen concentrations ranging from 40 to 80% (Fig. S25) at 600 °C. The current density at 1.3 V of LBCN9173 cell is 1.59, 1.56, and 1.64 A cm^{-2}, as hydrogen fraction is 80%, 60%, and 40%, respectively. The data indicates that hydrogen concentration has minimal influence on P-SOEC current density. This is likely because hydrogen, as a product, slightly impedes the HER reaction as its concentration rises.

As the best known to us, other alkaline earth metals, such as Sr, could be considered as A-site dopants and have a possibility of exhibiting high performances. $La_{0.9}Sr_{0.1}Co_{0.7}Ni_{0.3}O_{3-\delta}$ (LSCN9173) is characterized by the same experimental conditions with LBCN9173 and LCCN9173 (Figs. S26 and S27). LSCN9173 shows a current density of 0.95 A cm^{-2} at 1.3 V and 600 °C, which is inferior to those of LBCN9173 (1.58 A cm^{-2}) and LCCN9173 (1.1 A cm^{-2}). Additionally, as compared with other oxides containing Sr/Cs/La/Pr/Ce at A-site (Table S6), the performance of LBCN9173 cell still leads among them [57, 62, 70, 72, 73]. Encouragingly, our cell with LBCN9173 (1.58 A cm^{-2}) anode is comparable to or better than most of the reported anodes [14, 28, 29, 56, 57, 62–77], such as PNC (1.17 A cm^{-2}) [57], BCFZY (1.0 A cm^{-2}) [78], $Ba_{0.95}La_{0.05}(Fe_{0.8}Zn_{0.2})_{0.9}Ni_{0.1}O_{3-\delta}$ (BLFZN0.1, 0.67 A cm^{-2}) [73], and $Ba_{0.4}Sr_{0.5}Cs_{0.1}Co_{0.7}Fe_{0.2}Zr_{0.1}O_{3-\delta}$ (BSCsCFZr, 1.23 A cm^{-2}) [72]. These results strongly validate the superiority of Ba as an A-site dopant and further support the potential of LBCN9173 as a high-performance anode material for P-SOEC (Fig. 7g).

Figures 7d and S28 display the typical electrochemical impedance spectra (EIS) of the two cells under open circuit voltage (OCV) condition. Polarization resistance (R_p) and ohmic resistance (R_o) can be extracted from the difference of the low and high frequency intercepts of the EIS with the real axis and the high frequency intercept of the EIS with the real axis. The R_p of LBCN9173 cell is 0.394, 0.102, and 0.05 Ω cm^2 lowering 27%, 42%, and 44% than these of LCCN9173 cell at 550, 600, and 650 °C, respectively (Fig. 7e). Figure. 7f presents a comparison of R_p for this work and the state-of-art anodes [23, 35, 45, 56–61]. LBCN9173 cell exhibits a much lower R_p (0.102 Ω cm^2) at 600 °C compared to these anodes, such as BCCY (0.16 Ω cm^2) [59] and PBSCF (0.16 Ω cm^2) [35]. These excellent electrochemical performances in terms of current density and R_p of P-SOEC reinforce that LBCN9173 oxide is a highly effective anode for water electrolysis.

DRT analysis is an effective tool for decomposing complex and overlapped electrochemical processes into distinct or single processes by identifying the characteristic distribution of typical EIS timescales. In order to gain deeper insights into the water electrolysis reaction processes at the anode of the two cells, we employed DRT analysis on EIS measured at 550 and 600 °C. As illustrated in Fig. 8a, b, the electrochemical processes were deconvolved into 4 peaks, labeled P1, P2, P3, and P4. Among the four peaks, P1 corresponding to R_{LF} is related to O_2 desorption (step 5 in Table S7). P2 and P3 relevant to R_{IF} correspond to the H_2O adsorption/dissociation and O_2 formation processes (steps 1–4 in Table S7). P4 is associated with the charge transfer process, mirroring R_{HF} (step 6 in Table S7) (where LF, IF, and HF mean low frequency, intermediate frequency, and high frequency, respectively) [28]. The main difference in resistance between LBCN9173 and LCCN9173 cells lies in the IF resistances (Fig. 8c, d). R_{IF} of LBCN9173 cell with the values of 0.213 and 0.039 Ω cm^2 is lower than that of LCCN9173 cell (0.364 and 0.094 Ω cm^2) at 550 and 600 °C (Table S7), respectively, indicating faster reaction kinetics at LBCN9173 anode.

Water oxidation reaction (WOR) mainly relates to steps1-4, shown in Figs. 8e and S29a, and Table S7, whose Gibbs energies were calculated on the (001) surface of LBCN9173 and LCCN9173 models with 120 atoms (Figs. 8f and S29b-e). The results show that the rate-determined step of WOR for the two cells is the dissociation of H_2O (steps 1–2) (Fig. 8f). The calculating results align well with the DRT analysis (R_{IF} is much higher than R_{LF} shown in Fig. 8c, d and Table S7). The WOR energy barrier of LBCN9173 cell (3.39 eV) is lower than that of LCCN9173 cell (2.43 eV), which provides crucial insights into the superior electrochemical performances of LBCN9173 cell compared to LCCN9173 cell.

The EIS spectra of LBCN9173 and LCCN9173 cells under different oxygen partial pressures (p_{O2} = 10%, 20%, 40%) at 600 °C were analyzed for further exploring the anodic

https://doi.org/10.1007/s40820-025-01764-7

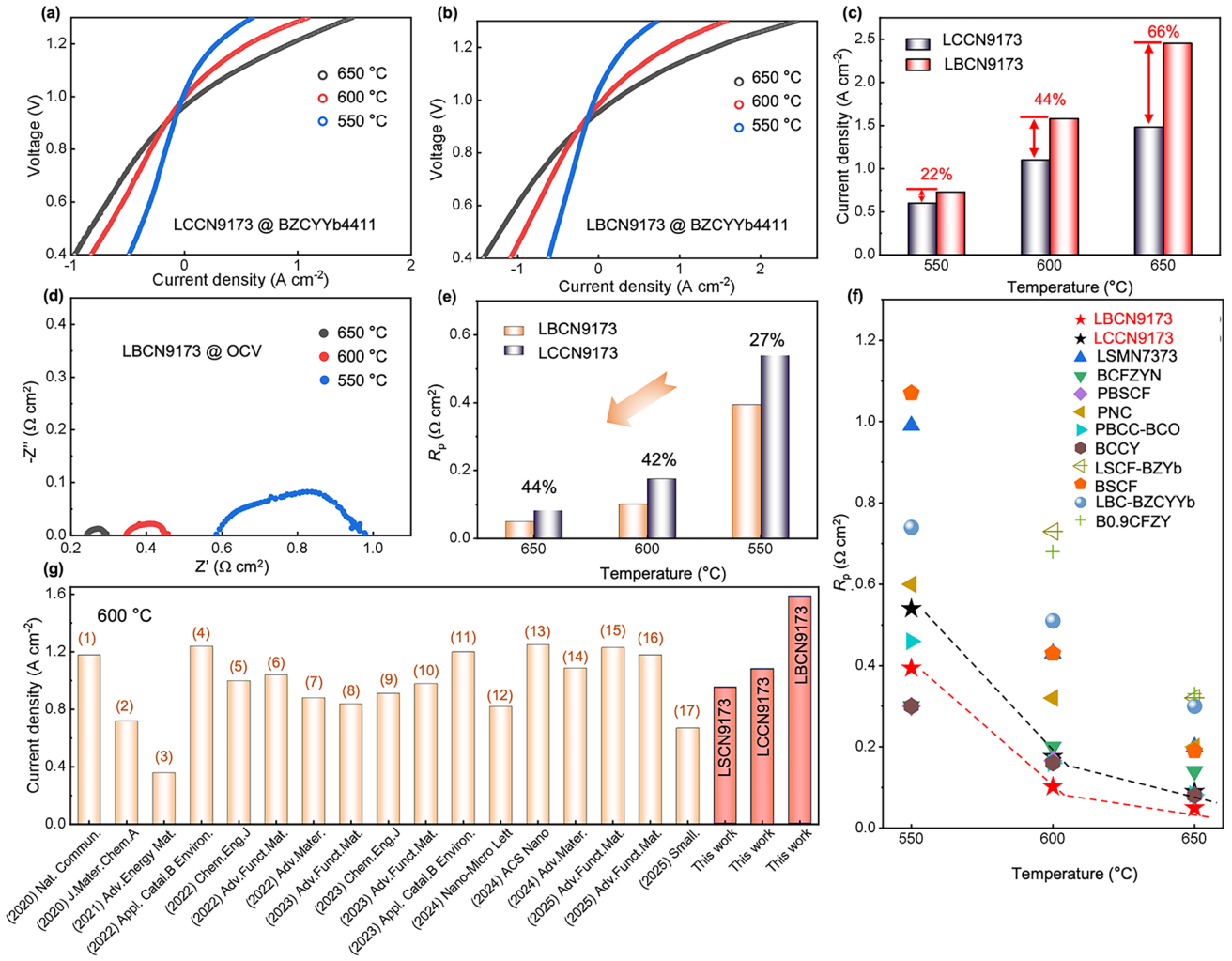

Fig. 7 Electrochemical performances of P-SOECs with LBCN9173 and LCCN9173 anodes. **a, b** I-V curves, **c** current densities at 1.3 V, **d** EIS, and **e** R_p for P-SOECs with LCCN9173 and LBCN9173 anodes. Summary of **f** R_p and **g** current densities at 1.3 V of this report and other state-of-art anodes. The compositions of oxides in **f**: LSMN7373 = $La_{0.7}Sr_{0.3}Mn_{0.7}Ni_{0.3}O_{3-\delta}$ [45], BCFZYN = $Ba_{0.95}(Co_{0.4}Fe_{0.4}Zr_{0.1}Y_{0.1})_{0.95}Ni_{0.05}O_{3-\delta}$ [56], PBSCF[35], $PrNi_{0.5}Co_{0.5}O_{3-\delta}$(PNC) [57], PBCC-BCO = $PrBa_{0.8}Ca_{0.2}Co_2O_{5+\delta}$–$BaCoO_{3-\delta}$ [58], BCCY = $BaCo_{0.7}(Ce_{0.8}Y_{0.2})_{0.3}O_{3-\delta}$ [59], LSCF6482-BZYb = $La_{0.6}Sr_{0.4}Co_{0.2}Fe_{0.8}O_{3-\delta}$–$BaZr_{0.8}Yb_{0.2}O_{3-\delta}$ [60], LBC-BZCYYb = $La_{0.6}Ba_{0.4}CoO_{3-\delta}$–$BaZr_{0.1}Ce_{0.7}Y_{0.1}Yb_{0.1}O_{3-\delta}$ [61], B0.9CFZY = $Ba_{0.9}Co_{0.4}Fe_{0.4}Zr_{0.1}Y_{0.1}O_{3-\delta}$ [23]. The oxides in **g** from left to right: (1) PNC [57], (2) $(PrBa_{0.8}Ca_{0.2})_{0.95}Co_2O_{6-\delta}$ [62], (3) $Sr_{0.9}Ce_{0.1}Fe_{0.8}Ni_{0.2}O_{3-\delta}$ [63], (4) $Ba(Co_{0.4}Fe_{0.4}Zr_{0.1}Y_{0.1})_{0.95}Mg_{0.05}O_{3-\delta}$ [64], (5) $Ba_{0.5}Sr_{0.5}(Co_{0.8}Fe_{0.2})_{0.95}P_{0.05}O_{3-\delta}$ [65], (6) $PrBaCo_{1.6}Fe_{0.2}Nb_{0.2}O_{5+\delta}$ [66], (7) LCCN7382 [29], (8) LCN91 [28], (9) $BaCo_{0.4}Fe_{0.4}Nb_{0.1}Sc_{0.1}O_{3-\delta}$ [67], (10) $Ba_{0.5}Sr_{0.5}(Co_{0.8}Fe_{0.2})_{0.9}Er_{0.1}O_{3-\delta}$ [68], (11) BCFZYN [56], (12) $Sr_{2.8}Fe_{1.8}Nb_{0.2}O_{7-\delta}$ [69], (13) $PrSrCo_{1.8}Nb_{0.2}O_{6-\delta}$ [70], (14) $Ba(Co_{0.4}Fe_{0.4}Zr_{0.1}Y_{0.1})_{0.95}Ni_{0.05}F_{0.1}O_{2.9-\delta}$ [71], (15) BSCsCFZr [72], (16) LCCFN-Cr [14], (17) $Ba_{0.95}La_{0.05}(Fe_{0.8}Zn_{0.2})_{0.9}Ni_{0.1}O_{3-\delta}$ [73].

reactions of P-SOEC. Shown in Fig. S30a, b, the R_p decreases from 0.161 to 0.086 Ω cm^2 (LBCN9173 cell) and 0.209 to 0.127 Ω cm^2 (LCCN9173 cell) as p_{O2} increased from 10 to 40%. The DRT analysis results suggest that the R_{IF} and R_{HF} show the same trend as the R_p. According to the function equation of $R = k(p_{O2})^{-n}$, the correlation coefficient (n) between resistance at different frequencies is calculated, as shown in Fig. S30c, d. The n values for both LBCN9173 (0.54 *vs* 0.37) and LCCN9173 (0.48 *vs* 0.25) cells in the IF range are greater than those in the HF range, indicating that the p_{O2} primarily affects the R_{IF} during the anodic reaction processes. Combined with the above DFT calculation result that R_{IF} is the critical reaction steps at the anode of the two P-SOECs, it is easy to infer that the $V_O^{\cdot\cdot}$ concentration has more effects on R_p. LBCN9173 oxide shows higher $V_O^{\cdot\cdot}$ concentration, and thus the lower R_p and the higher current densities (Figs. S8, S9

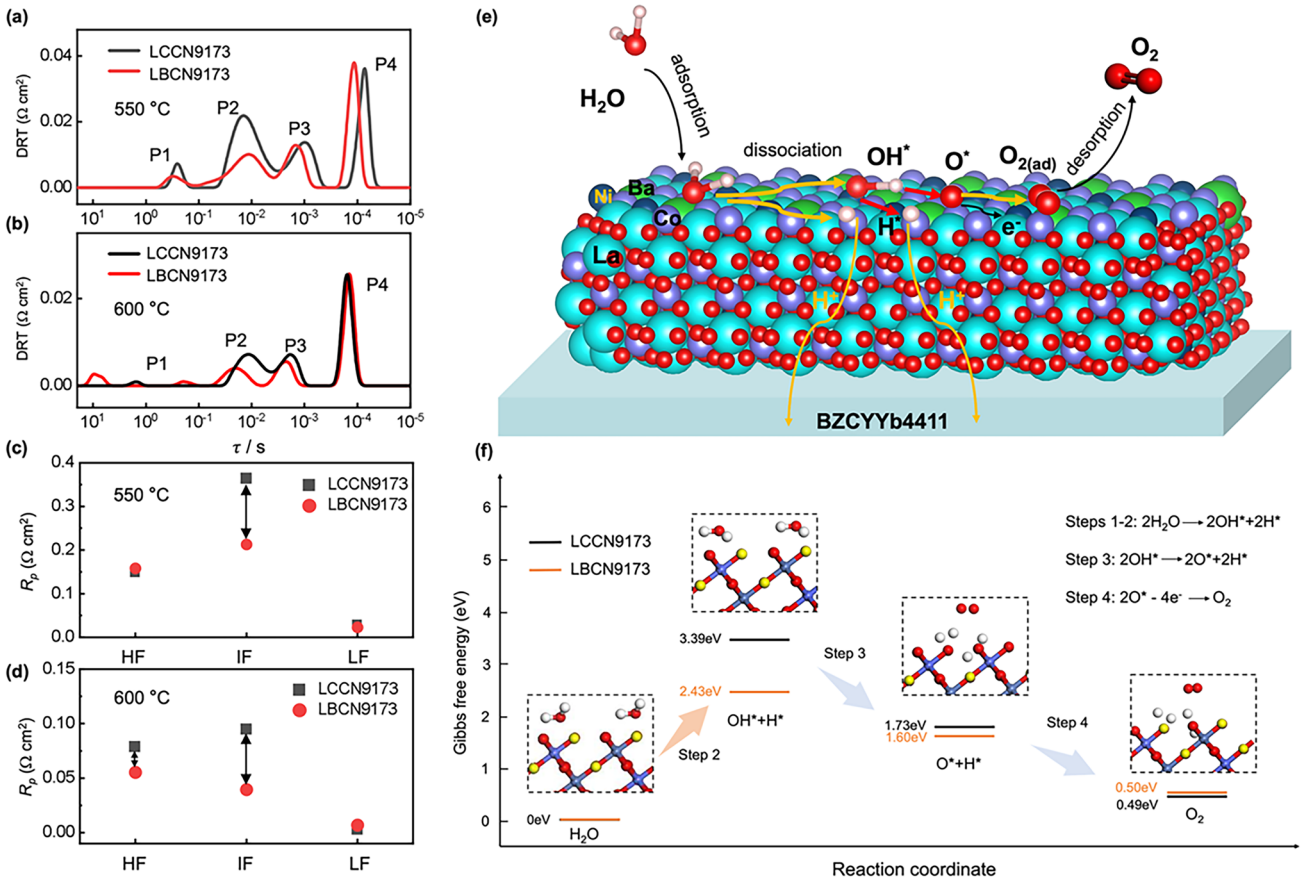

Fig. 8 **a, b** DRT plots and **c, d** R_{HF}, R_{IF}, and R_{LF} values for LBCN9173 and LCCN9173 cells under OCV condition at 550 and 600 °C. **e** Schematic WOR mechanism and **f** Gibbs free energy of main WOR steps on (001) surface of LBCN9173 anode

and Table S2). In conclusion, LBCN9173 oxide proves to be a high-performance anode for P-SOECs due to the synergistic enhancement of proton conductivity and catalytic activity. As illustrated in Fig. S31a, b**,** when the anode without or with low proton conductivity is used as the P-SOEC anode, the reaction active areas are confined to the triple-phase boundary (TPB) or result in ion accumulation at the reaction active sites, and thus the bad performance [59]. If the anode with high proton conductivity suffers in low catalytic activity, which will limit the generation of sufficient protons to the anode, thereby restricting the improvement of current density (Fig. S31c). Therefore, to achieve superior electrochemical performance, both rapid proton conductivity and efficient anode catalytic activity are indispensable [79]. As shown in Fig. S31d, the synergy between catalytic activity and proton conduction significantly enhances the overall performance of the P-SOEC. Overall, these results strongly suggest that the hydration ability of oxides can serve as an excellent indicator to screen the high-performance anode for P-SOECs by the ML model. Looking ahead, it is highly desired to develop a more sophisticated ML framework capable of simultaneously optimizing multiple key properties, particularly catalytic activity and proton conductivity. This advanced model will be trained on comprehensive datasets that incorporate diverse material characteristics, including oxygen vacancy concentration, ASR, proton conductivity, TEC, HPC, hydration enthalpy, etc. [25, 32, 80–82], enabling the identification of optimal oxide compositions and structures that effectively balance these required properties, and thus designing the high-performance anodes with more accuracy. This integrated approach will facilitate efficient exploration of complex oxide systems and accelerate the discovery of next-generation P-SOEC materials with unprecedented performances.

https://doi.org/10.1007/s40820-025-01764-7

4 Conclusion

In summary, $La_{0.9}Ba_{0.1}Co_{0.7}Ni_{0.3}O_{3-\delta}$ (LBCN9173) and $La_{0.9}Ca_{0.1}Co_{0.7}Ni_{0.3}O_{3-\delta}$ (LCCN9173) oxides were successfully synthesized and characterized, which were designed with the assistance of a well-constructed machine learning (ML) model. The experimental hydrated proton concentration (HPCs) of the two oxides matches well with the predicted values, manifesting a high reliability of the ML model. The HPC, hydration enthalpy, and hydration energy of LBCN9173 oxide are superior to those of LCCN9173 oxide. The high HPC (0.052 mol unit^{-1} at 500 °C), negative hydration energy (− 2.3 eV), and low proton conduction energy barrier (0.49 eV) enable the excellent proton conduction of LBCN9173 oxide. The lower free energies for oxygen evolution reaction (OER) processes of LBCN9173 oxide indicate the higher OER catalytic activity due to the higher oxygen vacancy concentration. As a result, P-SOEC with LBCN9173 anode exhibits the current densities of 1.58 and 2.45 A cm^{-2} at 1.3 V at 600 and 650 °C, respectively, higher than that of LCCN9173 cell (1.10 and 1.48 A cm^{-2}), which are superior to most of the reported P-SOECs. Overall, LBCN9173 oxide designed by the well-constructed ML model can serve as a promising anode for P-SOEC due to its outstanding proton conduction ability and high catalytic activity.

Acknowledgements This work was supported by National Natural Science Foundation of China (No. 12301626, No. 22409033, and No. 22409035), Guangdong Basic and Applied Basic Research Foundation (No. 2022A1515110612, No. 2022A1515110470 and No. 2024A1515011849), Funding by Science and Technology Projects in Guangzhou (No. 2025A03J3089 and No. 2024A04J4111), and Guangdong Engineering Technology Research Center for Hydrogen Energy and Fuel Cells.

Author Contributions Fangyuan Zheng and Baoyin Yuan are equally contributed to this work. Fangyuan Zheng: Investigation, Data curation, Writing-original draft. Baoyin Yuan: Software, Review, Funding acquisition. Huanxin Xiang and Youfeng Cai: Data curation. Xiting Zhang: Software. Ling Meng: Validation. Lei Du: Resources. Feng Jiao: Resources. Chunmei Tang: Review. Yoshitaka Aoki: Supervision. Ning Wang: Review, Supervision, Funding acquisition. Siyu Ye: Resources, Supervision, Funding acquisition.

Declarations

Conflict of interest The authors declare no interest conflict. They have no known competing financial interests or personal relationships that could have appeared to influence the work reported in this paper.

Supplementary Information The online version contains supplementary material available at https://doi.org/10.1007/s40820-025-01764-7.

References

1. Y. Wang, Y. Ling, B. Wang, G. Zhai, G. Yang et al., A review of progress in proton ceramic electrochemical cells: material and structural design, coupled with value-added chemical production. Energy Environ. Sci. **16**(12), 5721–5770 (2023). https://doi.org/10.1039/D3EE03121G
2. C. Tang, Y. Yao, N. Wang, X. Zhang, F. Zheng et al., Green hydrogen production by intermediate-temperature protonic solid oxide electrolysis cells: advances, challenges, and perspectives. InfoMat **6**(3), e12515 (2024). https://doi.org/10.1002/inf2.12515
3. H.A. Miller, K. Bouzek, J. Hnat, S. Loos, C.I. Bernäcker et al., Green hydrogen from anion exchange membrane water electrolysis: a review of recent developments in critical materials and operating conditions. Sustain. Energy Fuels **4**(5), 2114–2133 (2020). https://doi.org/10.1039/C9SE01240K
4. J.R. Varcoe, R.C.T. Slade, Prospects for alkaline anion-exchange membranes in low temperature fuel cells. Fuel Cells **5**(2), 187–200 (2005). https://doi.org/10.1002/fuce.200400045
5. S. Rauf, M.B. Hanif, Z. Tayyab, M. Veis, M.A.K. Yousaf Shah et al., Alternative strategy for development of dielectric calcium copper titanate-based electrolytes for low-temperature solid oxide fuel cells. Nano-Micro Lett. **17**(1), 13 (2024). https://doi.org/10.1007/s40820-024-01523-0
6. C. Yin, J. Yang, J. Feng, Y. Sun, Z. Liu et al., Tailoring the reversible phase transition of perovskite nanofiber electrodes for high-performance and durable reversible solid oxide cells. Nano-Micro Lett. **17**(1), 150 (2025). https://doi.org/10.1007/s40820-024-01600-4
7. C. Tang, K. Akimoto, N. Wang, L. Fadillah, S. Kitano et al., The effect of an anode functional layer on the steam electrolysis performances of protonic solid oxide cells. J. Mater. Chem.

A **9**(24), 14032–14042 (2021). https://doi.org/10.1039/D1TA02848K

8. C. Tang, N. Wang, R. Zhu, S. Kitano, H. Habazaki et al., Design of anode functional layers for protonic solid oxide electrolysis cells. J. Mater. Chem. A **10**(29), 15719–15730 (2022). https://doi.org/10.1039/D2TA02760G
9. Y. Cheng, S. Zhao, B. Johannessen, J.-P. Veder, M. Saunders et al., Atomically dispersed transition metals on carbon nanotubes with ultrahigh loading for selective electrochemical carbon dioxide reduction. Adv. Mater. **30**(13), 1706287 (2018). https://doi.org/10.1002/adma.201706287
10. Y.H. Kim, H. Jeong, B.R. Won, H. Jeon, C.H. Park et al., Nanoparticle exsolution on perovskite oxides: insights into mechanism, characteristics and novel strategies. Nano-Micro Lett. **16**(1), 33 (2023). https://doi.org/10.1007/s40820-023-01258-4
11. N. Wang, C. Tang, L. Du, R. Zhu, L. Xing et al., Advanced cathode materials for protonic ceramic fuel cells: recent progress and future perspectives. Adv. Energy Mater. **12**(34), 2201882 (2022). https://doi.org/10.1002/aenm.202201882
12. N. Wang, S. Hinokuma, T. Ina, H. Toriumi, M. Katayama et al., Incorporation of bulk proton carriers in cubic perovskite manganite driven by interplays of oxygen and manganese redox. Chem. Mater. **31**(20), 8383–8393 (2019). https://doi.org/10.1021/acs.chemmater.9b02131
13. S. Li, Z. Lü, B. Wei, X. Huang, J. Miao et al., A study of $(Ba_{0.5}Sr_{0.5})_{1-x}$ $SmxCo_{0.8}Fe_{0.2}O_{3-\delta}$ as a cathode material for IT-SOFCs. J. Alloys Compd. **426**(1–2), 408–414 (2006). https://doi.org/10.1016/j.jallcom.2006.02.040
14. X. Zhang, C. Tang, Y. Yang, F. Zheng, Q. Su et al., Novel high-entropy air electrodes enhancing electrochemical performances of reversible protonic ceramic cells. Adv. Funct. Mater. 2421083 (2025).https://doi.org/10.1002/adfm.202421083
15. G.C. Kostogloudis, C. Ftikos, Properties of A-site-deficient $La_{0.6}Sr_{0.4}Co_{0.2}Fe_{0.8}O_{3-\delta}$-based perovskite oxides. Solid State Ion. **126**(1–2), 143–151 (1999). https://doi.org/10.1016/S0167-2738(99)00230-1
16. B. Wei, Z. Lü, X. Huang, J. Miao, X. Sha et al., Crystal structure, thermal expansion and electrical conductivity of perovskite oxides Ba x Sr_{1-x} $Co_{0.8}Fe_{0.2}O_{3-\delta}$ ($0.3\leq$ x ≤ 0.7). J. Eur. Ceram. Soc. **26**(13), 2827–2832 (2006). https://doi.org/10.1016/j.jeurceramsoc.2005.06.047
17. F. Tietz, I. Arul Raj, M. Zahid, D. Stöver, Electrical conductivity and thermal expansion of $La_{0.8}Sr_{0.2}$(Mn, Fe, Co)$O_{3-\delta}$ perovskites. Solid State Ion. **177**(125), 1753–1756 (2006). https://doi.org/10.1016/j.ssi.2005.12.017
18. V.V. Kharton, E.N. Naumovich, A.A. Yaremchenko, F.M.B. Marques, Research on the electrochemistry of oxygen ion conductors in the former Soviet Union. J. Solid State Electrochem. **5**(3), 160–187 (2001). https://doi.org/10.1007/s100080000141
19. K. Singh, P.K. Addo, V. Thangadurai, J. Prado-Gonjal, B. Molero-Sánchez, $LaNi_{0.6}Co_{0.4-x}Fe_xO_{3-\delta}$ as air-side contact material for $La_{0.3}Ca_{0.7}Fe_{0.7}Cr_{0.3}O_{3-\delta}$ reversible solid oxide fuel cell electrodes. Crystals **12**(1), 73 (2022). https://doi.org/10.3390/cryst12010073
20. J. Dąbrowa, A. Olszewska, A. Falkenstein, C. Schwab, M. Szymczak et al., An innovative approach to design SOFC air electrode materials: high entropy La_{1-x}Srx(Co, Cr, Fe, Mn, Ni)$O_{3-\delta}$ (x = 0, 0.1, 0.2, 0.3) perovskites synthesized by the Sol–gel method. J. Mater. Chem. A **8**(46), 24455–24468 (2020). https://doi.org/10.1039/D0TA06356H
21. X. Xu, H. Wang, M. Fronzi, X. Wang, L. Bi et al., Tailoring cations in a perovskite cathode for proton-conducting solid oxide fuel cells with high performance. J. Mater. Chem. A **7**(36), 20624–20632 (2019). https://doi.org/10.1039/C9TA05300J
22. Z. Liu, Y. Bai, H. Sun, D. Guan, W. Li et al., Synergistic dual-phase air electrode enables high and durable performance of reversible proton ceramic electrochemical cells. Nat. Commun. **15**(1), 472 (2024). https://doi.org/10.1038/s41467-024-44767-5
23. R. Ren, Z. Wang, C. Xu, W. Sun, J. Qiao et al., Tuning the defects of the triple conducting oxide $BaCo_{0.4}Fe_{0.4}Zr_{0.1}Y_{0.1}O_{3-\delta}$ perovskite toward enhanced cathode activity of protonic ceramic fuel cells. J. Mater. Chem. A **7**(31), 18365–18372 (2019). https://doi.org/10.1039/C9TA04335G
24. Z. Luo, X. Hu, Y. Zhou, Y. Ding, W. Zhang et al., Harnessing high-throughput computational methods to accelerate the discovery of optimal proton conductors for high-performance and durable protonic ceramic electrochemical cells. Adv. Mater. **36**(18), 2311159 (2024). https://doi.org/10.1002/adma.202311159
25. S. Zhai, H. Xie, P. Cui, D. Guan, J. Wang et al., A combined ionic Lewis acid descriptor and machine-learning approach to prediction of efficient oxygen reduction electrodes for ceramic fuel cells. Nat. Energy **7**(9), 866–875 (2022). https://doi.org/10.1038/s41560-022-01098-3
26. B. Yuan, N. Wang, C. Tang, L. Meng, L. Du et al., Advances and challenges in high-performance cathodes for protonic solid oxide fuel cells and machine learning-guided perspectives. Nano Energy **122**, 109306 (2024). https://doi.org/10.1016/j.nanoen.2024.109306
27. X. Hu, Y. Zhou, Z. Luo, H. Li, N. Shi et al., Data-driven discovery of electrode materials for protonic ceramic cells. Energy Environ. Sci. **17**(23), 9335–9345 (2024). https://doi.org/10.1039/d4ee03762f
28. N. Wang, B. Yuan, F. Zheng, S. Mo, X. Zhang et al., Machine-learning assisted screening proton conducting Co/Fe based oxide for the air electrode of protonic solid oxide cell. Adv. Funct. Mater. **34**(12), 2309855 (2024). https://doi.org/10.1002/adfm.202309855
29. N. Wang, B. Yuan, C. Tang, L. Du, R. Zhu et al., Machine-learning-accelerated development of efficient mixed protonic–electronic conducting oxides as the air electrodes for protonic ceramic cells. Adv. Mater. **34**(51), 2203446 (2022). https://doi.org/10.1002/adma.202203446
30. R. Zohourian, R. Merkle, G. Raimondi, J. Maier, Mixed-conducting perovskites as cathode materials for protonic ceramic fuel cells: understanding the trends in proton uptake. Adv.

 https://doi.org/10.1007/s40820-025-01764-7

Funct. Mater. **28**(35), 1801241 (2018). https://doi.org/10.1002/adfm.201801241

31. K.D. Kreuer, S. Adams, W. Münch, A. Fuchs, U. Klock et al., Proton conducting alkaline earth zirconates and titanates for high drain electrochemical applications. Solid State Ion. **145**(1–4), 295–306 (2001). https://doi.org/10.1016/S0167-2738(01)00953-5
32. J. Hyodo, K. Tsujikawa, M. Shiga, Y. Okuyama, Y. Yamazaki, Accelerated discovery of proton-conducting perovskite oxide by capturing physicochemical fundamentals of hydration. ACS Energy Lett. **6**(8), 2985–2992 (2021). https://doi.org/10.1021/acsenergylett.1c01239
33. D. Hu, J. Kim, H. Niu, L.M. Daniels, T.D. Manning et al., High-performance protonic ceramic fuel cell cathode using protophilic mixed ion and electron conducting material. J. Mater. Chem. A **10**(5), 2559–2566 (2022). https://doi.org/10.1039/D1TA07113K
34. Y. Okuyama, T. Kozai, T. Sakai, M. Matsuka, H. Matsumoto, Proton transport properties of $La_{0.9}M_{0.1}YbO_{3-\delta}$ (M =Ba, Sr, Ca, Mg). Electrochim. Acta **95**, 54–59 (2013). https://doi.org/10.1016/j.electacta.2013.01.156
35. S. Choi, C.J. Kucharczyk, Y. Liang, X. Zhang, I. Takeuchi et al., Exceptional power density and stability at intermediate temperatures in protonic ceramic fuel cells. Nat. Energy **3**(3), 202–210 (2018). https://doi.org/10.1038/s41560-017-0085-9
36. R. Ren, Z. Wang, X. Meng, X. Wang, C. Xu et al., Tailoring the oxygen vacancy to achieve fast intrinsic proton transport in a perovskite cathode for protonic ceramic fuel cells. ACS Appl. Energy Mater. **3**(5), 4914–4922 (2020). https://doi.org/10.1021/acsaem.0c00486
37. I. Cho, J. Yun, B. Seong, J. Kim, S.H. Choi et al., Correlation between hydration properties and electrochemical performances on Ln cation size effect in layered perovskite for protonic ceramic fuel cells. J. Energy Chem. **88**, 1–9 (2024). https://doi.org/10.1016/j.jechem.2023.09.004
38. C. Duan, J. Tong, M. Shang, S. Nikodemski, M. Sanders et al., Readily processed protonic ceramic fuel cells with high performance at low temperatures. Science **349**(6254), 1321–1326 (2015). https://doi.org/10.1126/science.aab3987
39. N. Wang, H. Toriumi, Y. Sato, C. Tang, T. Nakamura et al., $La_{0.8}Sr_{0.2}Co_{1-x}Ni_xO_{3-\delta}$ as the efficient triple conductor air electrode for protonic ceramic cells. ACS Appl. Energy Mater. **4**(1), 554–563 (2021). https://doi.org/10.1021/acsaem.0c02447
40. C. Tang, B. Yuan, X. Zhang, F. Zheng, Q. Su et al., Rationally designed air electrode boosting electrochemical performance of protonic ceramic cells. Adv. Energy Mater. (2025). https://doi.org/10.1002/aenm.202402654
41. F. He, M. Hou, D. Liu, Y. Ding, K. Sasaki et al., Phase segregation of a composite air electrode unlocks the high performance of reversible protonic ceramic electrochemical cells. Energy Environ. Sci. **17**(11), 3898–3907 (2024). https://doi.org/10.1039/D4EE01608D
42. N. Shi, K. Zhu, Y. Xie, D. Huan, J. Hyodo et al., Investigation of water impacts on surface properties and performance of air-electrode in reversible protonic ceramic cells. Small **20**(36), 2400501 (2024). https://doi.org/10.1002/smll.202400501
43. L. Chen, G. Wang, K. Toyoura, D. Han, High-temperature protonic conduction in $La_2NiO_{4+\delta}$-based ruddlesden–popper type oxides: correlation with concentration of interstitial oxide ions. Small **20**(29), 2311473 (2024). https://doi.org/10.1002/smll.202311473
44. N. Wang, C. Tang, L. Du, Z.-Q. Liu, W. Li et al., Single-phase $La_{0.8}Sr_{0.2}Co_{1-x}$ $MnxO_{3-\delta}$ electrocatalyst as a triple H^+/O^{2-}/e-conductor enabling high-performance intermediate-temperature water electrolysis. J. Materiomics **8**(5), 1020–1030 (2022). https://doi.org/10.1016/j.jmat.2022.02.012
45. N. Wang, S. Hinokuma, T. Ina, C. Zhu, H. Habazaki et al., Mixed proton–electron–oxide ion triple conducting manganite as an efficient cobalt-free cathode for protonic ceramic fuel cells. J. Mater. Chem. A **8**(21), 11043–11055 (2020). https://doi.org/10.1039/D0TA03899G
46. R. Tang, X. Men, L. Zhang, L. Bi, Z. Liu, Bio-inspired honeycomb-shaped $La_{0.5}Sr_{0.5}Fe_{0.9}P_{0.1}O_{3-\delta}$ as a high-performing cathode for proton-conducting SOFCs. Int. J. Hydrog. Energy **48**(40), 15248–15257 (2023). https://doi.org/10.1016/j.ijhydene.2023.01.071
47. J. Dai, Y. Zhu, H.A. Tahini, Q. Lin, Y. Chen et al., Single-phase perovskite oxide with super-exchange induced atomic-scale synergistic active centers enables ultrafast hydrogen evolution. Nat. Commun. **11**(1), 5657 (2020). https://doi.org/10.1038/s41467-020-19433-1
48. X. Feng, Y. Wang, H. Zheng, P. Wang, X. Wang et al., Strategic potassium doping in perovskites: a pathway to superior oxygen reduction reaction and hydration activity in reversible proton ceramic electrochemical cells. J. Power. Sources **630**, 236136 (2025). https://doi.org/10.1016/j.jpowsour.2024.236136
49. X. Yang, G. Li, Y. Zhou, C. Sun, L. Bi, Tailoring $Pr_{0.5}Sr_{0.5}FeO_3$ oxides with Mn cations as a cathode for proton-conducting solid oxide fuel cells. Electrochem. Commun. **161**, 107685 (2024). https://doi.org/10.1016/j.elecom.2024.107685
50. Y. Liu, H. Huang, L. Xue, J. Sun, X. Wang et al., Recent advances in the heteroatom doping of perovskite oxides for efficient electrocatalytic reactions. Nanoscale **13**(47), 19840–19856 (2021). https://doi.org/10.1039/D1NR05797A
51. X. Lei, Z. Peng, P. Liang, D. Wu, X. Chao et al., Realizing oxygen ion conduction in perovskite structure $NaNbO_3$ by A-site Bismuth doping. J. Alloys Compd. **924**, 166506 (2022). https://doi.org/10.1016/j.jallcom.2022.166506
52. H. Zhang, W. Li, J. Essman, C. Quarti, I. Metcalf et al., Ultrafast relaxation of lattice distortion in two-dimensional perovskites. Nat. Phys. **19**(4), 545–550 (2023). https://doi.org/10.1038/s41567-022-01903-6
53. S. He, H. Dai, L. Bi, A highly efficient Sb-doped $La_{0.5}Sr_{0.5}FeO_{3-\delta}$ cathode for protonic ceramic fuel cells. Ceram. Int. **50**(1), 1284–1292 (2024). https://doi.org/10.1016/j.ceramint.2023.10.090
54. P. Yao, J. Zhang, Q. Qiu, G. Li, Y. Zhao et al., Design of a perovskite oxide cathode for a protonic ceramic fuel cell. Ceram.

Int. **50**(1), 2373–2382 (2024). https://doi.org/10.1016/j.ceramint.2023.11.015

55. K.D. Kreuer, Aspects of the formation and mobility of protonic charge carriers and the stability of perovskite-type oxides. Solid State Ion. **125**(1–4), 285–302 (1999). https://doi.org/10.1016/S0167-2738(99)00188-5
56. M. Liang, Y. Wang, Y. Song, D. Guan, J. Wu et al., High-temperature water oxidation activity of a perovskite-based nanocomposite towards application as air electrode in reversible protonic ceramic cells. Appl. Catal. B Environ. **331**, 122682 (2023). https://doi.org/10.1016/j.apcatb.2023.122682
57. H. Ding, W. Wu, C. Jiang, Y. Ding, W. Bian et al., Self-sustainable protonic ceramic electrochemical cells using a triple conducting electrode for hydrogen and power production. Nat. Commun. **11**(1), 1907 (2020). https://doi.org/10.1038/s41467-020-15677-z
58. Y. Zhou, E. Liu, Y. Chen, Y. Liu, L. Zhang et al., An active and robust air electrode for reversible protonic ceramic electrochemical cells. ACS Energy Lett. **6**(4), 1511–1520 (2021). https://doi.org/10.1021/acsenergylett.1c00432
59. Y. Song, Y. Chen, W. Wang, C. Zhou, Y. Zhong et al., Self-assembled triple-conducting nanocomposite as a superior protonic ceramic fuel cell cathode. Joule **3**(11), 2842–2853 (2019). https://doi.org/10.1016/j.joule.2019.07.004
60. K. Watanabe, Y. Yamaguchi, K. Nomura, H. Sumi, M. Mori et al., Effect of cobalt content on electrochemical performance for $La_{0.6}Sr_{0.4}Co_xFe_{1-x}O_{3-\delta}$ and $BaZr_{0.8}Yb_{0.2}O_{3-\delta}$ composite cathodes in protonic ceramic fuel cells. Ceram. Int. **49**(12), 21085–21090 (2023). https://doi.org/10.1016/j.ceramint.2023.03.105
61. H. Shimada, Y. Yamaguchi, H. Sumi, Y. Mizutani, Performance comparison of perovskite composite cathodes with $BaZr_{0.1}Ce_{0.7}Y_{0.1}Yb_{0.1}O_{3-\delta}$ in anode-supported protonic ceramic fuel cells. J. Electrochem. Soc. **167**(12), 124506 (2020). https://doi.org/10.1149/1945-7111/abab26
62. W. Tang, H. Ding, W. Bian, W. Wu, W. Li et al., Understanding of A-site deficiency in layered perovskites: promotion of dual reaction kinetics for water oxidation and oxygen reduction in protonic ceramic electrochemical cells. J. Mater. Chem. A **8**(29), 14600–14608 (2020). https://doi.org/10.1039/D0TA05137C
63. Y. Song, J. Liu, Y. Wang, D. Guan, A. Seong et al., Nanocomposites: a new opportunity for developing highly active and durable bifunctional air electrodes for reversible protonic ceramic cells. Adv. Energy Mater. **11**(36), 2101899 (2021). https://doi.org/10.1002/aenm.202101899
64. M. Liang, Y. Song, D. Liu, L. Xu, M. Xu et al., Magnesium tuned triple conductivity and bifunctionality of $BaCo_{0.4}Fe_{0.4}Zr_{0.1}Y_{0.1}O_{3-\delta}$ perovskite towards reversible protonic ceramic electrochemical cells. Appl. Catal. B Environ. **318**, 121868 (2022). https://doi.org/10.1016/j.apcatb.2022.121868
65. Z. Liu, D. Cheng, Y. Zhu, M. Liang, M. Yang et al., Robust bifunctional phosphorus-doped perovskite oxygen electrode for reversible proton ceramic electrochemical cells. Chem. Eng. J. **450**, 137787 (2022). https://doi.org/10.1016/j.cej.2022.137787
66. K. Xu, H. Zhang, Y. Xu, F. He, Y. Zhou et al., An efficient steam-induced heterostructured air electrode for protonic ceramic electrochemical cells. Adv. Funct. Mater. **32**(23), 2110998 (2022). https://doi.org/10.1002/adfm.202110998
67. C. Lu, R. Ren, Z. Zhu, G. Pan, G. Wang et al., $BaCo_{0.4}Fe_{0.4}Nb_{0.1}Sc_{0.1}O_{3-\delta}$ perovskite oxide with super hydration capacity for a high-activity proton ceramic electrolytic cell oxygen electrode. Chem. Eng. J. **472**, 144878 (2023). https://doi.org/10.1016/j.cej.2023.144878
68. Z. Liu, Y. Lin, H. Nie, D. Liu, Y. Li et al., Highly active nanocomposite air electrode with fast proton diffusion channels *via* Er doping-induced phase separation for reversible proton ceramic electrochemical cells. Adv. Funct. Mater. **34**(7), 2311140 (2024). https://doi.org/10.1002/adfm.202311140
69. N. Yu, I.T. Bello, X. Chen, T. Liu, Z. Li et al., Rational design of ruddlesden-popper perovskite ferrites as air electrode for highly active and durable reversible protonic ceramic cells. Nano-Micro Lett. **16**(1), 177 (2024). https://doi.org/10.1007/s40820-024-01397-2
70. K. Zhu, L. Zhang, N. Shi, B. Qiu, X. Hu et al., A superior catalytic air electrode with temperature-induced exsolution toward protonic ceramic cells. ACS Nano **18**(6), 5141–5151 (2024). https://doi.org/10.1021/acsnano.3c12609
71. X. Chen, N. Yu, Y. Song, T. Liu, H. Xu et al., Synergistic bulk and surface engineering for expeditious and durable reversible protonic ceramic electrochemical cells air electrode. Adv. Mater. **36**(32), 2403998 (2024). https://doi.org/10.1002/adma.202403998
72. Y. Zhang, Y. Wang, Z. Liu, Z. Wang, Y. Wang et al., Constructing robust and efficient ceramic cells air electrodes through collaborative optimization bulk and surface phases. Adv. Funct. Mater. **1**, 2422531 (2025). https://doi.org/10.1002/adfm.202422531
73. X. Yu, L. Ge, Y. Mi, B. Wu, Z. Yu et al., Superior active and durable air electrode for protonic ceramic cells by metal-oxide bond engineering. Small **21**(8), 2408607 (2025). https://doi.org/10.1002/smll.202408607
74. W. Wu, H. Ding, Y. Zhang, Y. Ding, P. Katiyar et al., 3D self-architectured steam electrode enabled efficient and durable hydrogen production in a proton-conducting solid oxide electrolysis cell at temperatures lower than 600 °C. Adv. Sci. **5**(11), 1800360 (2018). https://doi.org/10.1002/advs.201800360
75. S. Choi, T.C. Davenport, S.M. Haile, Protonic ceramic electrochemical cells for hydrogen production and electricity generation: exceptional reversibility, stability, and demonstrated faradaic efficiency. Energy Environ. Sci. **12**(1), 206–215 (2019). https://doi.org/10.1039/C8EE02865F
76. J.-S. Shin, H. Park, K. Park, M. Saqib, M. Jo et al., Activity of layered swedenborgite structured $Y0.8Er_{0.2}BaCo_{3.2}Ga_{0.8}O_{7+\delta}$ for oxygen electrode reactions in at intermediate temperature reversible ceramic cells. J. Mater. Chem. A **9**(1), 607–621 (2021). https://doi.org/10.1039/D0TA11000K

 https://doi.org/10.1007/s40820-025-01764-7

77. F. He, S. Liu, T. Wu, M. Yang, W. Li et al., Catalytic self-assembled air electrode for highly active and durable reversible protonic ceramic electrochemical cells. Adv. Funct. Mater. **32**(48), 2206756 (2022). https://doi.org/10.1002/adfm.202206756
78. C. Duan, R. Kee, H. Zhu, N. Sullivan, L. Zhu et al., Highly efficient reversible protonic ceramic electrochemical cells for power generation and fuel production. Nat. Energy **4**(3), 230–240 (2019). https://doi.org/10.1038/s41560-019-0333-2
79. Y. Cai, Y. Chen, M. Akbar, B. Jin, Z. Tu et al., A bulk-heterostructure nanocomposite electrolyte of $Ce_{0.8}Sm_{0.2}O_{2-\delta}$-$SrTiO_3$ for low-temperature solid oxide fuel cells. Nano-Micro Lett. **13**(1), 46 (2021). https://doi.org/10.1007/s40820-020-00574-3
80. Z. Li, X. Mao, D. Feng, M. Li, X. Xu et al., Prediction of perovskite oxygen vacancies for oxygen electrocatalysis at different temperatures. Nat. Commun. **15**(1), 9318 (2024). https://doi.org/10.1038/s41467-024-53578-7
81. Y. Cai, C. Wang, H. Yuan, Y. Guo, J.-H. Cho et al., Exploring negative thermal expansion materials with bulk framework structures and their relevant scaling relationships through multi-step machine learning. Mater. Horiz. **11**(12), 2914–2925 (2024). https://doi.org/10.1039/D3MH01509B
82. S. Han, B.G. Lee, D.-W. Lim, J. Kim, Machine learning-based prediction of proton conductivity in metal–organic frameworks. Chem. Mater. **36**(22), 11280–11287 (2024). https://doi.org/10.1021/acs.chemmater.4c02368